DIRECT NUMERICAL SIMULATION OF SUPERFLUID TURBULENCE

by

KARLA MORRIS

A dissertation submitted to the Graduate Faculty in Mechanical Engineering in partial fulfillment of the requirements for the degree of Doctor of Philosophy,
The City University of New York

2008

INFORMATION TO USERS

The quality of this reproduction is dependent upon the quality of the copy submitted. Broken or indistinct print, colored or poor quality illustrations and photographs, print bleed-through, substandard margins, and improper alignment can adversely affect reproduction.

In the unlikely event that the author did not send a complete manuscript and there are missing pages, these will be noted. Also, if unauthorized copyright material had to be removed, a note will indicate the deletion.

ProQuest LLC
789 East Eisenhower Parkway
P.O. Box 1346
Ann Arbor, MI 48106-1346

This manuscript has been read and accepted for the
Graduate Faculty in Engineering in satisfaction of the
dissertation requirement for the degree of Doctor of Philosophy.

	Joel Koplik
06 / 05 / 2008	
Date	Chair of Examining Committee
	Damian Rouson
06 / 05 / 2008	
Date	Co-Chair of Examining Committee
	Mumtaz Kassir
06 / 05 / 2008	
Date	Executive Officer

Yiannis Andreopoulos

Joseph Birman

Charles Watkins
Supervisory Committee

THE CITY UNIVERSITY OF NEW YORK

Abstract

DIRECT NUMERICAL SIMULATION OF

SUPERFLUID TURBULENCE

by

KARLA MORRIS

Adviser: Professor Joel Koplik

Co-Adviser: Damian Rouson

At low temperatures, as quantum effects become increasingly apparent, helium (He^4) transforms into a superfluid. The motion of superfluid helium (He II) can be decomposed into two interpenetrating components: (1) an inviscid (superfluid) liquid containing line vortices with quantized circulation and (2) a (normal fluid) gas of elementary thermal excitations. At sufficiently high driving velocities, the motion of He II becomes unstable and transitions to turbulence, commonly termed superfluid turbulence or quantum turbulence. A growing body of empirical evidence suggests that the macroscopic statistical behavior of quantum turbulence closely matches that of classical turbulence despite considerable differences in the physics at the mesoscopic scale of the inter-vortex spacing and the microscopic scale of the vortex core diameters [47,50]. Although a commonly used phenomenology involving quantum-vortex/normal-vortex locking has achieved some success in explaining the macroscopic similarities, current laboratory

measurements lack sufficient spatial resolution to verify vortex locking. The work presented here investigates the detailed mechanisms underlying quantum turbulence via direct numerical simulations (DNS) of superfluid vortex interactions with interpenetrating normal fluid turbulence. The driving fluid is the normal component which behaves as a statistically homogeneous isotropic turbulent flow, and both forced and decaying cases are simulated. The data obtained from the simulation is analyzed using wavelet transforms and velocity correlations. The normal fluid calculation employs a Navier-Stokes (NS) solver developed by Rouson and Xu [31] in a manner that facilitates rapid integration of new physics by expressing dynamical equations in forms very closely mirroring their analytical expression. The superfluid calculation employs a vortex filament method originated by Schwarz [39,40,41]. The Navier-Stokes and vortex filament equations are marched in time using a software module developed by Rouson, Morris and Xu [33] which facilitates rapid implementation of time advancement algorithms for coupled multi-physics problems.

Acknowledgments

I would first like to thank God for allowing me to get this far, and for always being by my side. There are many people in my life that have contributed, either directly or indirectly, to me getting to this point. Even though it is not possible to mention each and everyone individually, let my just say that I am eternally grateful to all those who have helped me through this process. To Mauricio, my best friend and husband, I am extremely grateful for your support through the dark moments, and your rejoicing through the bright ones, even though you never fully understood the subject of my work. To my girls, Kimaura and Kiandra, I appreciate you constantly reminding mommy of the bigger picture. A special thanks to my parents, Rolando and Rashida, for teaching me from an early age that with hard work I could achieve my full potential both academically and in life. To my sisters, Eslin and Elena, and my brother, Leyland, thank you for your unconditional love and support. To my best friend, Adriana, the sister I met ten years ago, there are not enough words to express how thankful I am for all that you do for me; you are a big part of my life. To my advisors, Damian Rouson and Joel Koplik, thank you for all the support, confidence, words of advice and wisdom. Thank you for showing me the way to the light on numerous occasions, and dragging me to the light in so many others. To all the members of the Mechanical Engineering Department at the City College of New York, thank you for all the help and support through my entire education process. A special thanks to Latif Jiji, Gary Benenson and Charles Watkins who have gone above and beyond to help me get to this point in life.

Table of Contents

List of Tables

List of Illustrations

Chapter 1

Introduction

All fluids exhibit quantum behavior at temperatures near absolute zero. In the case of substances that obey Bose-Einstein statistics quantum behavior results from the condensation of a substantial fraction of atoms into the ground energy level. At atmospheric pressure, however, most materials solidify before reaching such temperatures. In contrast, helium (He^4) remains liquid and exhibits behavior that can only be understood quantum mechanically. As helium is cooled below the lambda temperature T_λ=2.172K it displays *superfluidity* [13]. The motion of superfluid helium (He II) is of practical as well as fundamental interest. Of practical interest is the extremely high thermal conductivity of He II, which finds use in cooling superconducting devices. Of fundamental scientific interest is the mounting evidence that the macroscopic pressure and velocity statistics of turbulent He II closely match those of normal fluid turbulence, despite the microscopic differences between the two.

Not long after its discovery, a standard phenomenology was proposed by Tisza in 1940 [49] and by Landau in 1941 [18], to explain the special properties of He II as a two-fluid mixture. The two-fluid model describes the motion of He II as the superposition of normal fluid and superfluid components. The normal fluid component explains the viscous behavior of He II, while the superfluid component explains its inviscid behavior.

Based on this model, the superfluid component constitutes a background Euler fluid with an assembly of discrete vortex filaments with quantized circulation. These vortices interact with each other and with the surrounding gas of elementary thermal excitations comprising the normal fluid component. The two-fluid model proved successful in describing simple flows of He II [20].

At sufficiently high driving velocities, the motion of He II becomes unstable and turbulence ensues as energy is transferred from the normal fluid component to the superfluid component and a dense complex vortex tangle is formed. Superfluid turbulence, also known as quantum turbulence, is a turbulent flow at temperatures low enough to exhibit quantum effects. Considerable empirical evidence suggests classical and quantum turbulence have similar dynamical properties at large length scales, despite the dissimilarities at scales smaller than the inter-vortex spacing. Many attempts have been made to extend the two-fluid model to explain the surprising similarities by making analogies between aggregate quantum properties of the flow, e.g. locally averaged circulation, and their classical counterparts, e.g. the mean-square vorticity. Since the mean-square vorticity, or *enstrophy*, is known in classical turbulence theory to be proportional to the mean kinetic energy dissipation rate, one assumes by analogy that the locally averaged circulation in a quantum turbulent flow is proportional to its kinetic energy dissipation rate as well. And since the constant of proportionality in the classical case is the kinematic viscosity, the analogy leads naturally to an effective eddy viscosity in the quantum case. Although these propositions are supported by a picture of superfluid vortices "locking" in location and orientation with their normal fluid

counterparts, observing such fine details remains beyond current experimental capabilities [47,50]. Thus, while statistical data is consistent with the proposed phenomenology, only numerical simulation can truly confirm it and explore its limitations.

This project involves a numerical simulation of the dynamics of one-way coupled normal fluid and superfluid, accounting for the effects of mutual friction insofar as the superfluid reaction to the normal fluid but not the reverse. A fully-coupled calculation presents extreme computational difficulties due to the huge discrepancy in length scales between the superfluid vortex core size and the numerical resolution of any feasible normal fluid turbulence calculation. The direct numerical simulation (DNS) of the Navier-Stokes equation (NSE) generates statistically homogeneous, isotropic turbulence in the normal fluid. By definition, DNS solves NSE directly and ideally resolves all dynamically relevant scales of motion with no assumptions about the statistical properties of the turbulence. For classical turbulence, the results extracted from a DNS match experimental data for accessible Reynolds numbers. For quantum turbulence, the literature appears devoid of DNS studies of fully turbulent flows at finite temperatures, although there have been a few comparisons between experiments and solutions to the Gross-Pitaeski equation, which is formally valid at infinitesimal temperatures only [25].

In the current study, the superfluid motion is approximated via the vortex filament method, where each vortex is represented by a collection of discrete points connected by line segments. The motion of these points is governed by an equation that accounts for

the local and nonlocal contributions to the velocity induced upon one fluid element by another. The equation also incorporates the aforementioned mutual friction between the superfluid and normal fluid.

The current work increases our understanding of superfluid turbulence by providing a data set that can be probed at a level of detail greatly exceeding what is currently feasible in laboratory experiments. Chapter 2 of this dissertation gives a description of the two-fluid model and the equations of motion used to analyze superfluids. That chapter also includes a brief review of previous results obtained from experiments and simulations in superfluids. Chapter 3 presents the numerical methods used to solve the equations and the different physical considerations needed for the numerical simulation of superfluid turbulence. Chapter 4 incorporates some of the tests performed to validate and verify our code results by comparing it with published work and theoretical values. Chapter 5 presents the results obtained from our first case study: a Taylor-Green flow with no forcing. Chapter 6 includes results from simulations using an isotropic turbulent flow with linear forcing.

Chapter 2

Background on Superfluids

2.1 Superfluid Properties and Two-fluid Phenomenology

Figure 2.1 provides a helium (He^4) phase diagram. Helium I is a liquid that behaves as a Newtonian fluid. The lambda line drawn in Figure 2.1 marks the onset of Bose-Einstein condensation, which is responsible for the superfluid properties of He II. At a pressure of 0.05 atm, the lambda line yields the lambda temperature T_λ=2.172K. At T_λ, helium undergoes a second-order phase transition characterized in part by its infinite heat capacity and the absence of latent heat.

Below T_λ, He II exhibits numerous phenomena of quantum origin including [11]:

1. Although its viscosity is comparable to that of helium gas when measured between rotating disks, He II has no measurable viscosity when flowing through capillaries of 10^{-7} to 10^{-8} m diameter,
2. The superfluid component of He II has zero viscosity, zero entropy, and infinite thermal conductivity and thus cannot support temperature gradients. As a consequence, heat addition results in continuous evaporation rather than boiling.

3. He II creeps up and over the walls of an open container, creating a thin film of 30-nm thickness (a so-called Rollin film) until it reaches a place of higher temperature and evaporates [9].

The above phenomena involve interactions between He II and a solid boundary or source of heat. Since our focus is on the internal dynamics of quantum turbulence, the work presented here studies He II in the absence of solid boundaries at which the quantum vortex cores are known to attach and become pinned [41]. Furthermore, since heat transfer results in continual conversion of the condensed superfluid into the interpenetrating gaseous normal fluid, heat transfer results in so-called *counterflow* in which an effective superfluid flow towards the heated boundary is balanced by an effective normal fluid flow transporting heat away from the boundary. Since counterflow turbulence has no classical analogue, this work will consider isothermal flows only.

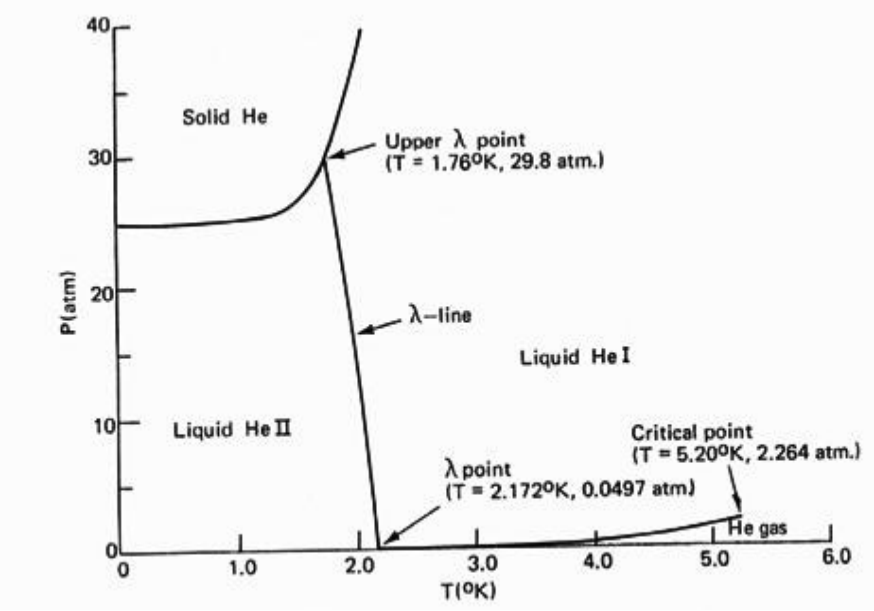

Figure 2.1: Phase diagram of Helium
Reprinted with permission from Seth J. Putterman, "Superfluid Hydrodynamics" (1974).
Copyright 1974, American Elsevier Pub. Co.

He II is actually one incompressible fluid with the distribution of atoms amongst the available energy levels determined by the temperature. Although superfluidity is associated with the behavior of the atoms populating the ground state, it would not be possible to extract those atoms preferentially without changing the fluid's temperature. Nonetheless it has proven fruitful historically to separate the *motion* of He II into superfluid and normal fluid components. A similar decomposition has a rich history in turbulence theory, where it is common to separate an ensemble-averaged velocity from the velocity fluctuation [27]. The fluctuating field is commonly referred to as the "turbulence", while the ensemble-averaged field is termed the "mean flow," despite the fact that both are characteristic of turbulent flow and neither would retain the same value in the absence of the other. In this study, there will be no mean flow, but the turbulence will be further decomposed according to the two-fluid model.

In the two-fluid model, the density of the superfluid and normal fluid components are designated ρ_s and ρ_n, respectively. Likewise, their velocities are $\mathbf{v}_s$ and $\mathbf{v}_n$. The total density and velocity are $\rho \equiv \rho_n + \rho_s$ and $\mathbf{v} \equiv \mathbf{v}_n + \mathbf{v}_s$. The ratio between the component densities varies nonlinearly with absolute temperature as shown in Figure 2.2. Two extremes are observed: He II is all superfluid at $T = 0K$ and all normal fluid at $T = T_\lambda$. The fraction of normal fluid is very nearly zero below $T = 1K$.

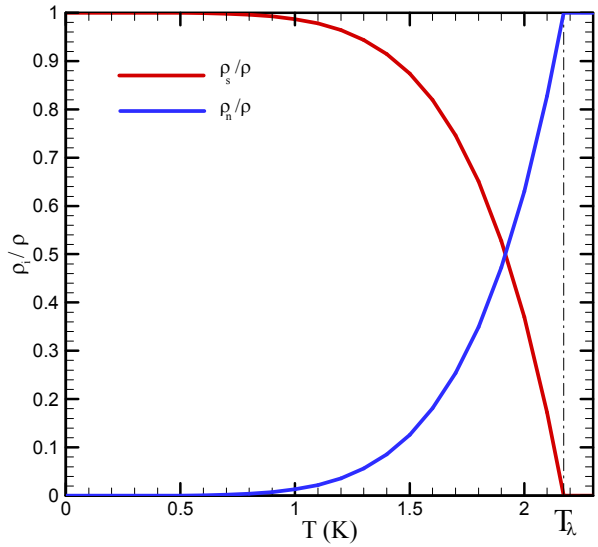

Figure 2.2: Density temperature dependence in He II at saturated vapor pressure

Some of the properties of He II that can be explained using the two-fluid model are

- The ability to flow through a microscopic channel with no apparent friction;
- The quantization of vortices where each vortex line has one quantum of the total fluid circulation;
- The ability to carry so-called *second sound* in addition to classical sound waves. Whereas classical sound waves are isentropic pressure oscillations in which the normal velocity ($\mathbf{v}_n$) and superfluid velocity ($\mathbf{v}_s$) move in phase, second sound is an isobaric entropy oscillation with antiphase motion of $\mathbf{v}_n$ and $\mathbf{v}_s$.

Although second sound is not modeled directly in this work, many of the results provide the first detailed calculation of properties that have been inferred from experimental measurements of second sound. Specifically, the attenuation of second sound as it passes through He II has been used to infer the quantum vortex line density present [50].

2.2 Superfluid Vortices

One of the first models of superfluid vortices was developed by Feynman, who assumed that superfluid vortices consisted of vortex filaments with quantized circulation and a core of atomic size. The vortex core was assumed hollowed and the superfluid circulated around it with a velocity given by $\mathbf{v}_s = \frac{\Gamma}{2\pi r}\vec{\theta} = \frac{h}{2\pi m r}\vec{\theta}$ along the axis of rotation in cylindrical coordinates (r,θ,z). Here *h* is Plack's constant, and *m* is the mass of one helium atom. This velocity is characteristic of that portion of a classical Rankine vortex in which the fluid is irrotational outside a core radius. By performing a balance between the energy per unit length of the vortex and the surface tension (σ=0.354 dyn/cm) Feynman calculated the core radius as $a \approx 0.5\,\text{Å}$. The energy of the vortex is estimated using the expression for the kinetic energy per unit length of a classical vortex in a potential flow $\varepsilon = \int_a^b \frac{1}{2}\rho_s \mathrm{v}_s^2 dr^2 = \rho_s \frac{\Gamma^2}{4\pi}\ln\left(\frac{b}{a}\right)$ where b is a characteristic length scale (radius of the container or mean distance between the vortices) [7,50]. Solutions to the nonlinear Schrodinger equation, which describe the zero-temperature limiting behavior of He II, suggest that the wavefunction vanishes inside the core [3]. This indicates that the core is evacuated of all material. Thus, from a continuum mechanics standpoint, any volume containing quantum vortices must be considered a multiply-connected domain.

Using the Madelung transformation, wherein the wavefunction $\psi(\mathbf{r},t)$ is expressed in terms of its amplitude $f(\mathbf{r},t)$ and phase $\varphi(\mathbf{r},t)$, the velocity of a single particle of mass *m* in a field of fixed potential is defined as $\mathbf{v}_s = \frac{\Gamma}{2\pi}\nabla\varphi = \frac{h}{2\pi m}\nabla\varphi$. In a multiply-connected

region, keeping ψ single-valued requires that φ change only by multiples of 2π so $\oint_c \nabla\varphi \cdot d\mathbf{l} = 2\pi n$ where $n = (0, \pm 1, \pm 2, \ldots)$.

In a simply connected region, the irrotational motion of the superfluid component implies that the circulation around any closed loop vanishes. However, when a quantum vortex passes through any surface bounded by the path of integration, the circulation integral is

$$\oint_c \mathbf{v}_s \cdot d\mathbf{l} = \frac{h}{2\pi m} \oint_c \nabla\varphi \cdot d\mathbf{l} = \frac{h}{m} n = \Gamma n$$

which restricts the circulation to quanta of $\Gamma = \frac{h}{m}$ [7]. Furthermore, single quantization is energetically favorable over multiple quantization, and experiments demonstrate that nature favors the nucleation of multiple vortices over the creation of one vortex with multiple quanta of circulation [7].

In He II, the vorticity of the superfluid component is confined to the interior of the superfluid vortices. In the absence of a mean flow, the superfluid motion is completely prescribed by the motion of these vortex cores and the motions they induce on surrounding fluid. When He II is placed in a rotating cylindrical vessel, for example, and the angular velocity of that vessel is increased past a critical value, a single quantum vortex filament nucleates and provides all of the vorticity of the flow. As the vessel's rotation rate increases, so does the number of vortex filaments. In this way the superfluid component mimics the solid body rotation of the normal fluid. The resulting collection of vortex lines is an unstable configuration. The inevitable perturbation of the vortex

lines' interactions with one another and with the surrounding normal fluid results in a random distributed vortex tangle [7].

Although no counterflow simulations were performed for this dissertation, counterflow turbulence experiments provide significant insights into the dynamics of superfluid turbulence. The experimental apparatus for thermal counterflow consists of a channel with one end closed and attached to a heater, while the other end is open to a helium bath. In superfluid He II, thermal energy is carried away from the source by the normal fluid at a rate of $W = \rho ST\mathbf{v}_n$. In the absence of net mass flow, $\rho_s \mathrm{v}_s + \rho_n \mathrm{v}_n$, due to the closed end, the superfluid velocity towards the heat source $\mathbf{v}_s = -\left(\rho_n / \rho_s\right)\mathbf{v}_n$ generates a counterflow velocity $\mathbf{v}_{ns} = \mathbf{v}_n - \mathbf{v}_s = W / \rho_s ST$. Turbulence occurs when the heat flux W supplied is higher that a critical value. At low counterflow velocities, there is dissipation due to the viscous interaction of the normal fluid with the walls of the channel. At higher velocities there is an additional dissipative process due to the mutual friction of the superfluid and normal fluid components [3]. Experiments by Vinen and Hall use the measurements of the attenuation of second sound in counterflow and rotating He II to show that this mutual friction is due to the presence of a vortex tangle that develops in superfluid turbulent flows. The mutual friction forces are the result of the interaction between the normal fluid component and the superfluid vortex tangle [50].

It has been found that nucleation of vortex lines occur when temperatures are close to T_λ or when the velocity of the flow is higher than the critical quantum turbulence velocity.

Complicated tangles result either from the stretching and reconnecting of interacting quantized vortices at temperatures below T_λ or from nucleation of quantized vortices formed by the remnants of classical vortices in an already turbulent flow that has been cooled past T_λ [50].

Schwarz produced the earliest numerical and analytical investigations of the superfluid vortex tangle dynamics with variable configurations. He showed that when a curvilinear vortex core approaches a surface up to a critical distance, a deformation occurs such that the vortex core tears and connects to the surface; after this connection, the two vortex ends move apart. His work included reconnection of vortex lines at flat surfaces with pinning sites. He also provided an analytical derivation of the velocity required to free the vortex line from the pinning site. A vortex with the depinning velocity is captured by the site, reconnects to the surface and then moves away [41]. Schwarz's numerical simulations consisted of a tangle of quantized vortex lines immersed in a superfluid and normal fluid flow with uniform velocity. In addition to the equation of motion of the vortex tangle, the simulation modeled the reconnection of lines that cross each other [42].

2.3 Superfluid Turbulence Experiments

Helium has an extremely low kinematic viscosity (three orders of magnitude smaller than air), which offers the possibility of obtaining higher Reynolds numbers in experiments with smaller models and flow velocities than are possible in most fluid mechanics laboratory settings. However, because of the lack of fundamental understanding helium is not currently used as a high Reynolds number test fluid. Several groups have

performed experiments to gain insight into the promising potential of He II for scale experiments.

Smith et. al. [44] conducted experiments to calculate the drag on a sphere immersed in flowing He I and He II as a function of the Reynolds number based on the measured pressure distribution along the surface of the sphere. In the case of He I at T=2.54K, clearly supercritical (turbulent) behavior was observed for Reynolds numbers ranging from 1.6×10^5 to 4.3×10^5 with boundary separation at about 110^o in all cases. For He II at T=1.8K, boundary layer separation likewise occurred at 110^o which is within the observed range in classical turbulent flows pass a sphere (65^o-145^o) [1]. In this case, Smith et. al. was able to obtain an obvious drag crisis at Reynolds numbers from 1.7×10^5 to 9.6×10^5 based on the sphere diameter of 10mm.

Experiments by Choi et. al. [6] extended the work of Smith et. al. by looking at the temperature dependence of the critical Reynolds number and the magnitude of the drag crisis. The data show the crisis occurs at approximately the same Reynolds number for all temperatures, and that the drag coefficient in He II increases with decreasing temperature. The minimum drag coefficient reach in the crisis was also shown to increase with decreasing temperature. However, by using dynamical similarity arguments applied to the two-fluid equations, they defined a modified Reynolds number involving the factor $1 - \frac{\rho_s}{\rho}$. They showed minimum values of the drag coefficients for He II at the same modified Reynolds number for each temperature. This modified Reynolds number was found to be of the same order as the minimum classical drag crisis Reynolds number.

Stalp et al. developed a theoretical model for the energy spectrum in decaying isotropic turbulence in classical fluids. The model accounts for the growth of the large length scale characterizing energy containing eddies and its saturation as the eddies reach a size comparable to the container size. The model not only described classical experiments on decaying turbulence created by a steadily oscillating grid in a tank of water (where for fully developed turbulence, the assumed spectrum distribution is reasonable), but it also described the decay of grid turbulence in superfluid He II as obtained in experiments where 4 orders of magnitude of vorticity are observed [46]. The theoretical model of decaying grid turbulence assumes a turbulent energy spectrum of the form $E(k) = Ak^m$ for small wavenumbers where both theory and experiments have found m=2 with constant A. In the case of large wave numbers, a Kolmogorov spectrum is adopted where $E(k) = C\varepsilon^{2/3}k^{-5/3}$ and C is a dimensionless constant. The two spectral forms meet at wavenumber $k_e(t) = 2\pi/l_e(t)$ which corresponds to the peak value for the energy spectrum of the energy containing eddies of length scale $l_e(t)$. Besides the usual truncation of the spectrum at large wavenumbers $k > k_\eta$, where k_η is the Kolmogorov wavenumber, the model also included the truncation of the spectrum at $k < k_c$ where the critical wavenumber $k_c = 2\pi/d$ is related to the size of the container *d*.

Stalp et al. also investigated dissipation at small length scales in superfluid grid turbulence. They used the attenuation of second sound to measure the vortex line density in the superfluid component. The measurements tracked the rate at which the length of the line decays with time. Experimental results were shown to agree with a quasi-

classical model developed for grid turbulence in a classical fluid. At steady state, where $E(k)$ is independent of time, the nonlinear inertial terms of the NSE are responsible for the energy transfer down the cascade. In the inertial range, where the Reynolds number is high and the dissipation due to viscosity is extremely low, the rate of energy passed from the small wavenumbers to the large wave numbers is a constant ε. The energy spectrum in this region is a Kolmogorov spectrum. This spectrum is cut off at even higher wavenumbers where the Reynolds numbers approaches unity and the dissipation due to viscosity becomes important. In this region, the energy dissipation is $\varepsilon = \nu\langle\omega^2\rangle$. The model assumes that at length scales large compare to the inter-vortex spacing, superfluid He II behaves as a classical fluid with the total density of helium with the superfluid and normal fluid motions locked in unison. As such, the kinetic energy dissipation rate of the superfluid component follows the same Kolmogorov spectrum. Under these assumptions, the experimental data was used to calculate a temperature-dependent effective viscosity (ν') for the superfluid component. This effective viscosity describes the rate of energy flow through the cascade in a Kolmogorov spectrum with $\varepsilon = \nu'\langle\kappa L^2\rangle$ [47].

The Stalp et al. experiments on grid turbulence in superfluid He II employed a grid of unconventional design, consisting of 4 parallel rectangular tines crossed by a single tine at a 45^0 angle. This design was originally used because of the small size of the channel and concerns regarding the structural integrity of the grid as it is moved at high speeds through the flow. Niemela et al. [24] repeated the experiments done by Stalp et al. with a different grid design similar to the ones used in classical turbulence experiments. The

temperature dependence and magnitude of the effective viscosity proved comparable to the results previously obtained [46,47].

2.4 Superfluid Turbulence Numerical Simulations

Among the numerical simulation results that support the similarities in the statistics of classical turbulence and quantum turbulence are those obtained by Nore et. al. [25], who studied decaying superfluid turbulence in He II below 1K. These temperatures are low enough to consider the normal fluid component negligible, which supports their use of the Nonlinear Schrödinger Equation (NLSE), also known as the Gross-Pitaevskii Equation [25]. Nore et al. compared the results obtained from numerical simulations of a Taylor-Green (TG) vortex in a superfluid flow to simulation results from TG vortex in viscous fluid using the NSE. They found excellent agreement in the energy dissipation rate of the TG superfluid flow and the incompressible, viscous TG flow. In particular, the moment at which the maximum energy dissipation occurred $t_{\max}$ and the value of the energy dissipation rate $\varepsilon(t_{\max})$ also agreed. In addition, they found that $t_{\max}$ and $\varepsilon(t_{\max})$ depend weakly on the coherent length in the superfluid flow case. They also found that under similar experimental conditions, the Taylor microscale for He I at T=5.174K and P=2.2 10^5 Pa agrees in order of magnitude with the average distance between neighboring vortices in He II at T=1K [25].

Numerical simulations of superfluid turbulence at T=0K where no normal fluid is present have shown the existence of a Kolmogorov energy spectrum for length scales larger compare to the inner vortex spacing. These findings contradict the argument that in superfluid He II the Kolmogorov energy spectrum is due to the presence of the normal

fluid component [2]. Numerical experiments by Barenghi et al. [4] included one-way coupled numerical simulations wherein the superfluid is driven by a time-independent normal fluid velocity field that takes the form of an Arnold-Beltrami-Childress (ABC) velocity field:

$$\begin{aligned} v_n^x &= A\sin(2\pi z/\lambda) + C\cos(2\pi y/\lambda) \\ v_n^y &= B\sin(2\pi x/\lambda) + A\cos(2\pi z/\lambda) \\ v_n^z &= C\sin(2\pi y/\lambda) + B\cos(2\pi x/\lambda) \end{aligned}$$

which represents a periodic array of vortical motions with varying orientation. Although greatly simplified relative to the broad range of length and time scales of turbulent flow, the ABC flow draws some inspiration from visualizations of experiments in turbulent water by Schwarz [43]. During the experiment, small scale structures, that were later shown to be regions of concentrated vorticity, were observed. In computer simulations of classical turbulence, these regions manifest as spontaneous appearances of extended vortex tubes with finite length, with motion perpendicular to their axes. The numerical simulation results show how in the presence of mutual friction and vortex wave instabilities, the flow evolved into a vortex tangle with a higher filament density and a configuration exhibiting a clear alignment of the superfluid vortex filaments along the normal fluid vortices[4].

Kivotides et al. [15] improved these approximations by using a Kinematic Simulation (KS) model for the imposed normal fluid field. The introduced normal fluid flow field was given by $\mathbf{v_n} = \mathbf{U}_n^0 + \mathbf{v}'_n$ where $\mathbf{U}_n^0$ is the uniform flow, and $\mathbf{v}'_n$ is the turbulent

fluctuation of the form $\mathbf{v}'_n = \sum_{m=1}^{M}\left[\mathbf{A}_m \times \hat{\boldsymbol{k}}_m \cos(\boldsymbol{k}_m \cdot \mathbf{x} + \omega_m t) + \mathbf{B}_m \times \hat{\boldsymbol{k}}_m \sin(\boldsymbol{k}_m \cdot \mathbf{x} + \omega_m t)\right]$.

Here M=64 is the number of modes, $\hat{\boldsymbol{k}}_m$, $\mathbf{A}_m$, and $\mathbf{B}_m$ are random vectors such that $\boldsymbol{k}_m = k_m \hat{\boldsymbol{k}}_m$ and $|\mathbf{A}_m|^2 = |\mathbf{B}_m|^2 = \left(2/3\right) E_n(k_m)\Delta k_m$. The normal fluid energy spectrum obeys the Kolmogorov scaling law $E_n(k_m) \approx \varepsilon^{2/3} k_m^{-5/3}$ and mass continuity $\nabla \cdot \mathbf{v}'_n = 0$. The frequency of each mode is equal to the eddy turnover time $\omega_m = \sqrt{k_m^3 E_n(k_m)}$. The time-dependent velocity field produced by the KS model is a more realistic approximation to the properties observed in turbulent flow. It was found that at T=0K when there is purely superfluid the energy spectrum followed a power law similar to k_m^{-1}. However, in the case of the simulation at T=1.3K, at which point there is a very low fraction of normal fluid present, the total energy spectrum obeyed the Kolmogorov spectrum $k_m^{-5/3}$ [15].

Later work by Kivotides [16] found the same quantum vortex clustering in regions of high normal fluid vorticity when using a different driving force for the superfluid. He generated the newer driving force from a snapshot of a statistically isotropic, turbulent state held constant in time while the superfluid evolved.

Fully coupled simulations are computationally very expensive and have been attempted only for very simple geometries. Two-dimensional flow configurations tracked the changes to a stationary normal fluid flow in the presence of three different superfluid filaments structures: a single line vortex, four line vortices, and four rotating line vortices.

Three dimensional flows include the motion of a superfluid ring in stationary normal fluid. In this configuration, it was observed that the normal fluid near the superfluid filament was dragged resulting in the formation of two normal fluid rings one with the same orientation as the superfluid ring and the other oriented in the opposite direction [12].

2.5 Mathematical Model

(a) Governing Equation of the Normal Fluid Component

Since the normal fluid component provides all of the viscosity of He II, its motion is governed by the incompressible form of the NSE supplemented by the continuity equation for mass conservation:

$$\begin{aligned} \nabla \cdot \mathbf{v}_n &= 0 \\ \frac{\partial \mathbf{v}_n}{\partial t} + \mathbf{v}_n \cdot \nabla \mathbf{v}_n &= -\frac{1}{\rho}\nabla P + \nu_n \nabla^2 \mathbf{v}_n + \frac{\rho_s}{\rho}\mathbf{f} \end{aligned} \tag{2.1}$$

where $\mathbf{v}_n(\mathbf{x},t)$ and $P(\mathbf{x},t)$ are the normal fluid velocity vector and pressure at position $\mathbf{x} \in \Omega$ and time $t \in (0,T]$; $\mathbf{f}(\mathbf{x},t)$ is the mutual friction force between the superfluid and normal fluid components; and ρ and ν_n are the constant fluid density and kinematic viscosity. The first equation in (2.1) guarantees mass conservation. The second equation in (2.1) is a statement of Newton's second law of motion for an infinitesimal element of incompressible fluid obeying a Newtonian constitutive relation. This dissertation's focus on one-way coupling between the normal fluid and superfluid which implies the last term in equation (2.1) is neglected. A fully-coupled calculation would involve severe computational difficulties due to the huge disparity in length scales between the

superfluid vortex core size and the numerical resolution of any feasible normal fluid turbulence calculation.

Since our concern is the internal dynamics of the turbulence, it will suffice to assume a periodically repeated, cubical domain $\Omega \equiv [0,2\pi)^3$. Periodic boundary conditions are assumed to have negligible influence on the internal dynamics so long as the domain size exceeds the length over which the dependent variables are statistically correlated. Similarly, the time interval will be chosen to greatly exceed the time over which the dependent variables are statistically correlated. It is expected that these choices will provide sufficient samples of the largest and longest-surviving turbulence structures to obtain accurate statistics.

(b) Governing Equation of the Superfluid Component

Due to its irrotational nature and the absence of viscosity and entropy, the superfluid component behaves similarly to a classical, inviscid Euler fluid. The irrotationality of Euler fluids implies their velocity can be expressed as a gradient of a potential function, $\phi(\mathbf{x},t)$. The incompressible statement of mass conservation in equation (2.1) requires such a potential to satisfy the Laplace equation, $\nabla^2\phi = 0$. The linearity of this equation suggests that fluid velocity fields can be constructed by superposition. It is common to construct classical potential flow solutions by distributing singularities on flow boundaries. It is natural therefore to model the superfluid component by distributing a line vortex along each vortex core.

Each line vortex is represented by a curve $\mathbf{s} = \mathbf{s}(\xi, t)$, where ξ is arclength and t is time. Each point on the vortex line experiences two forces: a Magnus lift force ($\mathbf{f}_M$) and a frictional drag force ($\mathbf{f}_D$). The Magnus force arises from the circulation of the superfluid vortex line in the irrotational superfluid. Requiring the superfluid wave function to be single valued leads to a requirement that circulation around a superfluid vortex be quantized. The quantum of circulation is $\Gamma \equiv \frac{h}{m}$, where h is Planck's constant and m is helium's atomic mass [7]. The Magnus lift force is then

$$\begin{aligned} \mathbf{f}_M &= \rho_s \Gamma \mathbf{s}' \otimes \left(\mathbf{v}_L - \mathbf{v}_{s,total} \right) \\ \mathbf{v}_{s,total} &= \mathbf{v}_i + \mathbf{v}_s \end{aligned} \tag{2.2}$$

where $\mathbf{v}_L$ is the velocity of the vortex line and $\mathbf{v}_{s,total}$ is the total velocity of the superfluid surrounding the vortex; $\mathbf{v}_s$ results from externally opposed pressure gradients or boundary conditions (excluding vortex contributions); and $\mathbf{v}_i$ is the velocity induced by other vortex lines and other parts of the same vortex line. An interesting consequence of the quantization of vorticity is that quantum vortices do not experience the vorticity enhancement via vortex stretching that is of critical importance in normal fluid turbulence.

The drag force results from the mutual friction between the superfluid and the normal fluid. The interaction between a normal fluid and a vortex filament in relative motion produce the mutual friction force

$$\mathbf{f}_D = -\alpha \rho_s \Gamma \mathbf{s}' \otimes \left[\mathbf{s}' \otimes \left(\mathbf{v}_n - \mathbf{v}_{s,total} \right) \right] - \alpha' \rho_s \Gamma \mathbf{s}' \otimes \left(\mathbf{v}_n - \mathbf{v}_{s,total} \right) \tag{2.3}$$

Since the vortex core diameter is of atomic scale ($a_0 \approx 10^{-8} cm$), the effective mass predicted by potential flow theory is insignificant. Since its actual mass is also negligible, a force balance yields $\Sigma \mathbf{F} = \mathbf{f}_M + \mathbf{f}_D = \mathbf{0}$. Solving this equation for the vortex line velocity yields

$$\frac{d\mathbf{s}}{dt} = \mathbf{v}_s + \mathbf{v}_i + \alpha \mathbf{s}' \otimes \left(\mathbf{v}_n - \mathbf{v}_s - \mathbf{v}_i\right) + \alpha' \mathbf{s}' \otimes \left[\mathbf{s}' \otimes \left(\mathbf{v}_n - \mathbf{v}_s - \mathbf{v}_i\right)\right] \tag{2.4}$$

The current DNS will track every line vortex in the superfluid by equation (2.4).

Chapter 3

Numerical Methods

3.1 The Navier-Stokes Solver

The computer simulations performed for this dissertation use the NSE solver described by Rouson and Xu [31], who recently developed a novel, layered design strategy in which the layer that describes the physics employs continuous, grid-free expressions of the NSE very closely mirroring their analytical form in (2.1). The requisite algebraic and differential operators are defined in a spatial representation layer that facilitates Fourier spectral approximation without exposing any information regarding the data types, values and layout, nor the numerical methods that operate on that data. Hiding such implementation details facilitates rapid integration of new physics such as that to be described in the next section.

The NSE was marched forward in time using a software module developed by Rouson, Morris and Xu [33] which allowed for rapid addition of new time advancement algorithms without direct access to the data being advanced. The time integration module allows the user to choose amongst several advancement algorithms. The algorithms in this dissertation employed herein are a low-storage, third-order Runge-Kutta algorithm developed by Spalart, Moser and Rogers [45] and the fourth-order Runge-Kutta method described in Section 3.4.

3.2 Calculating Spatial Derivatives in the Vortex Equation of Motion

The derivatives of vortex point position vectors are approximated using a second-order accurate central finite difference equation. Because of the non-uniformity of the vortex point spacing, the derivatives of $\mathbf{s}$ in terms of arclength (ξ) are easier to calculate by parameterizing with an artificial counter function (*f*) that takes on integer values at each vortex point (see Figure 3.1) [38]. This parameterization coupled with the fact that $\mathbf{s}'$ is a unit vector yields the following equation:

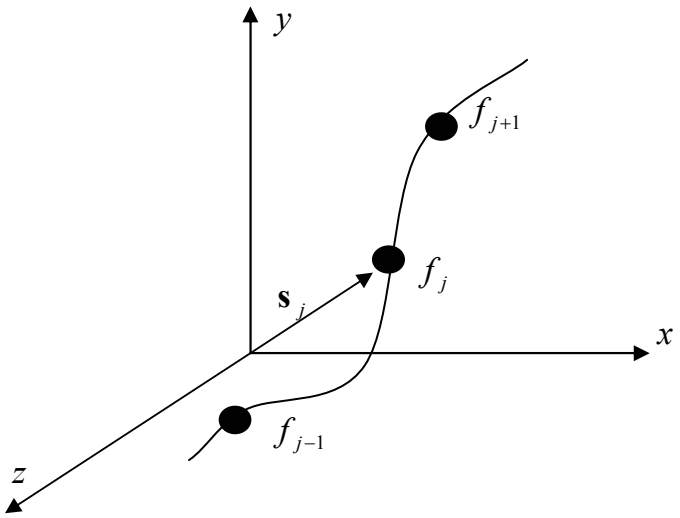

Figure 3.1: Vortex filament vector representation using a counter function (f) to parameterize the curve.

$$\begin{aligned}
&\mathbf{s}(\xi) = \mathbf{s}(f) \\
&\mathbf{s}_i = \mathbf{s}(f_i) = x_i\vec{e}_x + y_i\vec{e}_y + z_i\vec{e}_z \\
&|\mathbf{s}'| = \left|\frac{d\mathbf{s}}{d\xi}\right| = \left|\frac{d\mathbf{s}}{df}\frac{df}{d\xi}\right| = 1 \text{ therefore } \left|\frac{d\mathbf{s}}{df}\right| = \left(\frac{df}{d\xi}\right)^{-1}
\end{aligned} \tag{3.1}$$

which further yields the second derivative

$$\mathbf{s}'' = \frac{d^2\mathbf{s}}{d\xi^2} = \frac{d^2\mathbf{s}}{df^2}\left|\frac{d\mathbf{s}}{df}\right|^{-2} - \left|\frac{d\mathbf{s}}{df}\right|^{-3}\left(\frac{d^2\mathbf{s}}{df^2} \bullet \frac{d\mathbf{s}}{df}\right)\mathbf{s}' \tag{3.2}$$

The final expressions for the derivatives are obtained by substituting the central finite difference approximation of $\frac{d\mathbf{s}}{df}$ into equations (3.1)-(3.2):

$$\begin{aligned}
\mathbf{s}' &= \frac{(x_{i+1}-x_{i-1})\vec{e}_x + (y_{i+1}-y_{i-1})\vec{e}_y + (z_{i+1}-z_{i-1})\vec{e}_z}{\sqrt{(x_{i+1}-x_{i-1})^2 + (y_{i+1}-y_{i-1})^2 + (z_{i+1}-z_{i-1})^2}} \\
\mathbf{s}'' &= \frac{(x_{i+1}-2x_i+x_{i-1})\vec{e}_x + (y_{i+1}-2y_i+y_{i-1})\vec{e}_y + (z_{i+1}-2z_i+z_{i-1})\vec{e}_z}{\left[(x_{i+1}-x_{i-1})^2 + (y_{i+1}-y_{i-1})^2 + (z_{i+1}-z_{i-1})^2\right]^{4}} \\
&- \left\{ \begin{bmatrix} (x_{i+1}-2x_i+x_{i-1})(x_{i+1}-x_{i-1}) + \\ (y_{i+1}-2y_i+y_{i-1})(y_{i+1}-y_{i-1}) + \\ (z_{i+1}-2z_i+z_{i-1})(z_{i+1}-z_{i-1}) \end{bmatrix} \left[\frac{(x_{i+1}-x_{i-1})\vec{e}_x + (y_{i+1}-y_{i-1})\vec{e}_y + (z_{i+1}-z_{i-1})\vec{e}_z}{\left[(x_{i+1}-x_{i-1})^2 + (y_{i+1}-y_{i-1})^2 + (z_{i+1}-z_{i-1})^2\right]^{4^2}} \right] \right\}
\end{aligned} \tag{3.3}$$

3.3 Approximating the Biot-Savart Law

The induced velocity is calculated by approximating the Biot-Savart law:

$$\mathbf{v}_i(\mathbf{r}) = \frac{\Gamma}{4\pi}\int \frac{(\mathbf{s}-\mathbf{r})\otimes d\mathbf{s}}{|\mathbf{s}-\mathbf{r}|^3} \tag{3.4}$$

where the integration should be carried out along the vortex filament. Since the integrand is singular at $\mathbf{s}=\mathbf{r}$, we divide the integration process into two parts: (1) a local contribution involving only the point of interest, *j* ,and its neighbors, *j+1* and *j-1* and (2) a nonlocal contribution including all other points. The local contribution is calculated by integrating over a circular path without including the j+1, j and j-1 points. The result is subtracted from the expression of the total induced velocity experienced by a single vortex ring to get the following [42]:

$$\mathbf{v}_i^{local}(\mathbf{r}) = \frac{\Gamma}{4\pi}(\mathbf{s}'\otimes\mathbf{s}'')Ln\left(\frac{2\sqrt{l_- l_+}}{e^{1/4}a_0}\right) \tag{3.5}$$

The nonlocal induced velocity is calculated by integrating over piece-wise linear segments between two vortex points [37]. With the result

$$\begin{aligned}
&\mathbf{v}_i^{nonlocal}(\mathbf{r}) = \sum_{k=1}^{N} \frac{\Gamma}{4\pi} \frac{\left(|\mathbf{R}_k| + |\mathbf{R}_{k+1}|\right)\left(\mathbf{R}_k \otimes \mathbf{R}_{k+1}\right)}{\left(|\mathbf{R}_k||\mathbf{R}_{k+1}|\right)\left(|\mathbf{R}_k||\mathbf{R}_{k+1}| + \mathbf{R}_k \cdot \mathbf{R}_{k+1}\right)} \\
&k \neq j+1, j, j-1 \\
&\mathbf{R}_{k+1} = \mathbf{s}_{k+1} - \mathbf{r} \\
&\mathbf{R}_k = \mathbf{s}_k - \mathbf{r}
\end{aligned} \tag{3.6}$$

where the total nonlocal induced velocity is the sum of the contributions from all nonlocal points in the simulation.

3.4 Superfluid Time Advancement: Adaptive Fourth-Order Runge-Kutta

Choosing a time-advancement algorithm involves trade-offs between accuracy, stability, cost and convenience. Explicit methods offer the convenience of avoiding iterations on nonlinear problems. Unlike explicit multi-step methods, Runge-Kutta methods additionally offer the convenience of being self-starting and potentially lower costs from not having to store solution values from previous timesteps. Amongst Runge-Kutta methods, the fourth-order methods provide less restrictive stability limits than the lower-order methods but fewer function evaluations per order of accuracy than the higher-order methods. Finally, Runge-Kutta-Fehlberg methods allow for adaptive step-size control based on error estimation. The fourth-order Runge-Kutta-Fehlberg method employs an error estimation based on comparison to a fifth-order method. We refer to this scheme as RKF45.

In order to advance the solution to a differential equation of the form $dy/dt = f(t_i, y_i)$ from time t_n to time $t_{n+1} \equiv t_n + h$, the RKF45 method employs six functions evaluations [22]:

$$
\begin{aligned}
K_1 &= hf(t_i, y_i) \\
K_2 &= hf\left(t_i + \frac{1}{4}h, y_i + \frac{1}{4}K_1\right) \\
K_3 &= hf\left(t_i + \frac{3}{8}h, y_i + \frac{3}{32}K_1 + \frac{9}{32}K_2\right) \\
K_4 &= hf\left(t_i + \frac{12}{13}h, y_i + \frac{1932}{2197}K_1 - \frac{7200}{2197}K_2 + \frac{7296}{2197}K_3\right) \\
K_5 &= hf\left(t_i + h, y_i + \frac{439}{216}K_1 - 8K_2 + \frac{3680}{513}K_3 - \frac{845}{4104}K_4\right) \\
K_6 &= hf\left(t_i + \frac{1}{2}h, y_i - \frac{8}{27}K_1 + 2K_2 - \frac{3544}{2565}K_3 + \frac{1859}{4104}K_4 - \frac{11}{40}K_5\right)
\end{aligned}
\tag{3.7}
$$

A solution of 4th-order accuracy is then constructed by combining four of the evaluations:

$$y_{i+1}^{RK4} = y_i + \frac{25}{216}K_1 + \frac{1408}{2565}K_3 + \frac{2197}{4101}K_4 - \frac{1}{5}K_5 \tag{3.8}$$

while a 5th-order accurate solution is constructed by combining five evaluations:

$$y_{i+1}^{RK5} = y_i + \frac{16}{135}K_1 + \frac{6656}{12825}K_3 + \frac{28561}{56430}K_4 - \frac{9}{50}K_5 + \frac{2}{55}K_6 \tag{3.9}$$

A nice feature of RKF45 is the ability to reuse each of the function evaluations from the fourth-order approximation in constructing the fifth-order one.

At each time step, the step size is adjusted according to

$$h_0 = \begin{cases} Sh_1 \left| \frac{\Delta_0}{\Delta_1} \right|^{0.20} & \Delta_0 \geq \Delta_1 \\ Sh_1 \left| \frac{\Delta_0}{\Delta_1} \right|^{0.25} & \Delta_0 \langle \Delta_1 \end{cases} \tag{3.10}$$

where S is a safety factor slightly smaller than the unity, Δ_0 is the maximum allowable error, Δ_1 is the estimated error, h_0 is the desired time step for the next approximation and h_1 is the time step used in the current approximations [28].

Our dependent variables, the components of **s**, are an oscillatory functions. They pass through zero and are bounded from above by the size of the computational box on a side. Therefore, the maximum error is defined as $\Delta_0 = \varepsilon\lambda$, where ε is a defined tolerance and λ is the size of the simulation box side. Following a procedure similar to that of Press et al. [28,29], we never increase h by more than a factor of 5 and we never reduce it by more than a factor of 10.

The superfluid validation efforts discussed in Chapter 4 employ the RKF45 method. All the simulations results shown in Chapter 4 correspond to superfluid He II in which the normal fluid component is either non-existant ($T << T_\lambda$) or is moving with a constant velocity field.

3.5 Normal Fluid Time Advancement: Low-Storage Third-Order Runge-Kutta

In the case of the normal fluid, the NSE were advanced through time using a semi-implicit, third-order Runge-Kutta (RK3) scheme first published by Spalar, Moser and Rogers [45]. This method decomposes the time derivative into linear and nonlinear operators:

$$\frac{\partial \mathbf{u}}{\partial t} = \mathbf{L}(\mathbf{u}) + \mathbf{N}(\mathbf{u}) \tag{3.11}$$

where $\mathbf{L}$ and $\mathbf{N}$ are time-independent linear and nonlinear operators, respectively. These vector-valued differential operators act on a vector function $\mathbf{u}$. In the case of the normal fluid component $\mathbf{L}$ includes the viscous term and $\mathbf{N}$ the convection term. The scheme advances $\mathbf{u}$, from $\mathbf{u}_i$ at time t to $\mathbf{u}_{i+1}$ at time $t + \Delta t$ in three sub-steps:

$$\begin{aligned}
\mathbf{u}' &= \mathbf{u}_i + \Delta t\left[\mathbf{L}\left(\alpha_1 \mathbf{u}_i + \beta_1 \mathbf{u}'\right) + \gamma_1 \mathbf{N}_i\right] \\
\mathbf{u}'' &= \mathbf{u}' + \Delta t\left[\mathbf{L}\left(\alpha_2 \mathbf{u}' + \beta_2 \mathbf{u}''\right) + \gamma_2 \mathbf{N}' + \zeta_1 \mathbf{N}_i\right] \\
\mathbf{u}''' &= \mathbf{u}'' + \Delta t\left[\mathbf{L}\left(\alpha_3 \mathbf{u}'' + \beta_3 \mathbf{u}_{i+1}\right) + \gamma_3 \mathbf{N}'' + \zeta_2 \mathbf{N}'\right]
\end{aligned} \tag{3.12}$$

Equations (3.12) advance the linear terms with an implicit method similar to the second-order accurate Crank-Nicolson algorithm and the convective terms with an explicit method analogous to a second-order accurate Adams-Bashforth algorithm. The coefficients shown in equation (3.13) are determined to obtain very nearly third order Runge-Kutta scheme (second order for the viscous terms and third order for convective and cross terms) [45]:

$$\begin{aligned}
\gamma_1 &= \frac{8}{15}, \quad \gamma_2 = \frac{5}{12}, \quad \gamma_3 = \frac{3}{4}, \\
\alpha_1 &= \frac{29}{96}, \quad \alpha_2 = -\frac{3}{10}, \quad \alpha_3 = \frac{1}{6}, \\
\beta_1 &= \frac{37}{160}, \quad \beta_2 = \frac{5}{24}, \quad \beta_3 = \frac{1}{6}, \\
\zeta_1 &= -\frac{17}{60}, \quad \zeta_2 = -\frac{5}{12}
\end{aligned} \tag{3.13}$$

The main advantages of this method lie in its ability to provide the third-order accuracy and minimum storage requirements of an explicit method even though the linear terms are advanced implicitly.

By analogy with the linear advection/diffusion equation, one can derive a time step restriction that preserves stability of the numerical approximation to the Navier-Stokes equations. One can write this restriction in terms of the dimensionless Courant-Friedrichs-Lewy (CFL) number:

$$CFL \equiv \frac{2}{3}\pi\left[\frac{|u|}{\Delta x} + \frac{|v|}{\Delta y} + \frac{|w|}{\Delta z}\right]\Delta t \le \sqrt{3} \tag{3.14}$$

where u, v, and w are the maximum velocity components in each direction and Δx, Δy, and Δz are the grid spacing in each direction.

3.6 Time Advancement of the Governing Equations

The source codes for each fluid component were developed separately with the superfluid code employing the RKF45 scheme and the normal fluid code the RK3 scheme. In order to time advance both components in a consistent manner, either the normal fluid

calculation must be adapted to RKF45 or the superfluid calculation must be adapted to RK3. Each approach harbors pitfalls: advancing the normal fluid with an explicit scheme such as RKF45 imposes severe stability restrictions [23]; while advancing the superfluid with RK3 requires a methodology for adapting the time step to preserve stability and accuracy. Yet, unlike the rich history of applying linearization to generate the CFL stability condition for the Navier-Stokes equations, the literature appears to contain no fully deductive theory for the numerical stability of the nonlinear superfluid vortex equation of motion (2.4). (The choice of RKF45 and its success in our study was driven largely by the experience of previous authors [4,12,37] and the accumulated wisdom acquired by tuning the algorithm's parameters to avoid well-known instability modes.) This subsection describes the approach chosen to resolve this dilemma.

In the case of simulations where both the normal fluid and the superfluid components are allowed to evolve over time, the timestep Δt used must satisfying the stability restrictions of both components. The first test was to advance the two components using two different schemes. A timestep was determined for the superfluid component Δt_s using RKF45, and a separate timestep was found for the normal fluid component Δt_n with RK3. Both components were then advanced using $\Delta t \equiv \min(\Delta t_s, \Delta t_n)$. It was observed after running a number of simulations that the more restrictive timestep was always the normal fluid. A subsequent test was performed where the superfluid was advanced through time using RKF45 for a given normal fluid configuration (an instantaneous snapshot from a normal fluid DNS) with a timestep that satisfied the CFL condition. It was found that the resulting Δt_n never exceeded Δt_s. These tests each

support the conclusion that both components can be stably advanced using the timestep determine by the normal fluid component. All combined simulations reported in this dissertation employed this assumption to set the time step.

3.7 Remeshing of Vortex Filament

Choosing the number of mesh points to represent the superfluid vortices involves a balance of subtle issues related to spurious reconnections, cost, numerical accuracy, and stability. Section 3.8 will address reconnections. Regarding cost, the non-local induced velocity calculation dominates the superfluid calculation budget with $N_s(N_s - 1)$ interactions between N_s points. In any reasonable approximation to superfluid turbulence, the number of superfluid points greatly exceeds the number of normal fluid grid points (N_n) in each flow direction. Since the 3D FFT calculations dominate the normal fluid calculation and carry a $N_n^3 \log N_n$ cost, the superfluid calculation dominates the overall DNS operation count.

Regarding numerical accuracy and stability, in the apparent absence of any published error estimates or stability bounds for the quantum turbulence problem, we created our remeshing criterion based on the apparent best practices of those who have studied quantum vortex dynamics. Ultimately, the validation of these practices comes in the avoidance of obvious numerical artifacts such as oscillations at the shortest resolvable wavelengths and in reproducing the physics simulated by more fundamental calculations. In Section 4.3, we compare our results to solutions of the nonlinear Schrodinger equation published by Koplik and Levine [17].

Qualitatively, one expects the mesh density required for a given level of accuracy to increase with vortex curvature. We ensure sufficient resolution by maintaining a mesh spacing δ proportional to the local radius of curvature R, setting $\delta = \frac{2\pi R}{32}$. Although this increases the mesh density in regions of small curvature, the absolute number of mesh points required to resolve a specific feature remains scale-invariant. For example, 32 points are used to represent a circle, independent of its radius. Remeshing is achieved by defining a range of allowable radii of curvature [37]. We use $R_{\max} = \frac{\lambda}{2}$ and $R_{\min} = \frac{\lambda}{20}$. We also define a maximum and minimum proportionality constant for the length scale ($\theta_{\max} = \frac{4\pi}{32}$ and $\theta_{\min} = \frac{\pi}{32}$). The simulation thus resolves length scales on the range of $\theta_{\min} R \le \delta \le \theta_{\max} R$. While $\theta_{\min}$ sets the maximum resolution, $\theta_{\max}$ helps to prevent non-physical reconnections as is described in section 3.8. Similar parameters have been used before by other authors [4], however, the algorithm follow for both removal and addition of points we developed during the course of this project.

We take three conditions as being individually necessary and jointly sufficient for point removal. Upon defining $\delta_{m+1,m} \equiv \left\| \mathbf{s}_{m+1} - \mathbf{s}_m \right\| \quad \forall m$, the removal of a point j (see Figure 3.2) requires

$$\left(\delta_{j+1,j} < \theta_{\min} R_j \quad \vee \quad \delta_{j,j-1} < \theta_{\min} R_{j-1}\right)$$

$$\wedge \left(\delta_{j+1,j} + \delta_{j,j-1} < \theta_{\max} R_{\max}\right)$$

$$\wedge\left(\delta_{j+1,j}+\delta_{j,j-1}<\theta_{\max}R_j\right)$$

where $\vee$ and $\wedge$ are Boolean "or" and "and," respectively; while R_j and R_{j-1} are the local radius of curvature at point j and $j-1$ correspondingly. Removing points based on the first condition enforces a maximum local resolution (minimum spacing), while enforcing the second and third conditions ensures a minimum local resolution (maximum spacing) after removal.

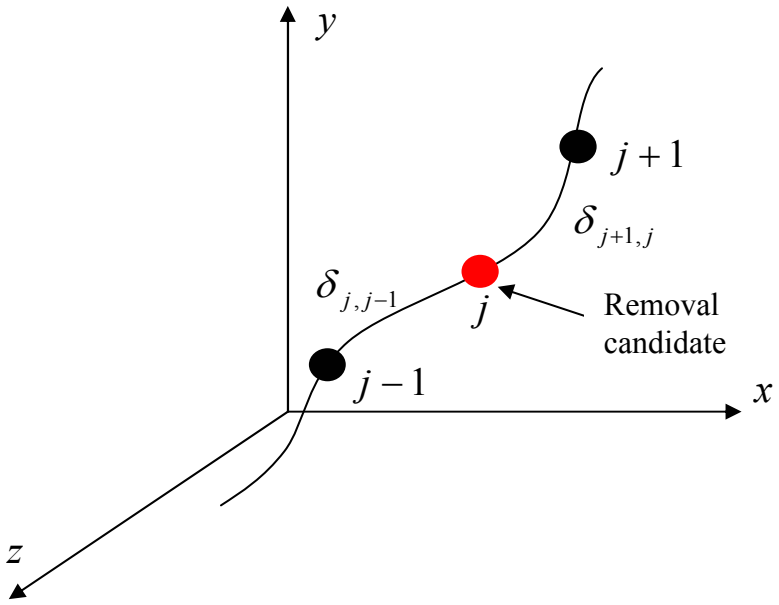

Figure 3.2: Arclength representation of vortex filament with conditions to remove vortex point

Similarly, we take three conditions as individually necessary and jointly sufficient for point insertion. Defining $R_{avg}\equiv\frac{R_j+R_{j+1}}{2}$, we write the three conditions for the insertion of point k (see Figure 3.3):

$$\left(\delta_{k,j}\rangle\theta_{\min}R_j \quad\wedge\quad \delta_{j+1,k}\rangle\theta_{\min}R_{avg}\right)$$

$$\wedge\left(\delta_{j+1,j}>\theta_{\min}R_{\min}\right)$$

$$\wedge\left(\delta_{j+1,j} > \theta_{\max} R_{avg}\right)$$

where R_{avg} is used to approximate the curvature at point k. Much like with point removal, inserting points based on the first condition enforces a maximum local resolution (minimum spacing) after insertion, while the second condition avoids violating the maximum resolution (minimum spacing) limit before insertion. The third condition ensures that minimum local resolution (maximum spacing) is satisfied before point addition.

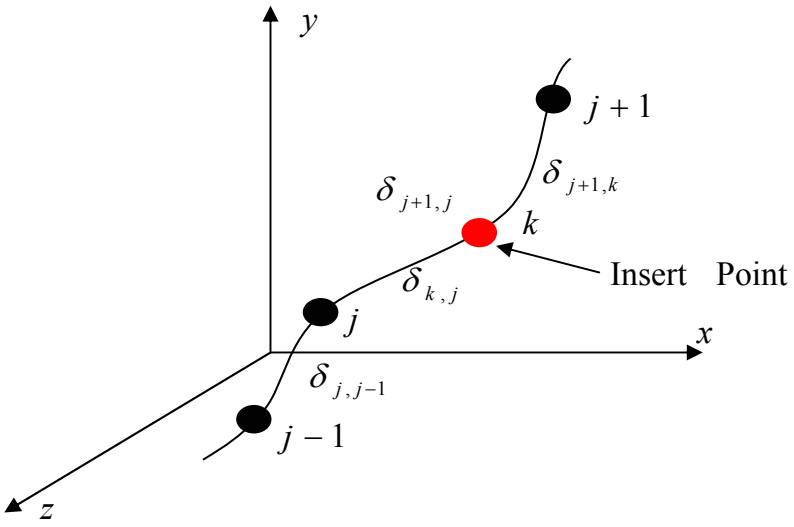

Figure 3.3: Arclength representation of vortex filament with conditions to add vortex point

Additional point removal occurs when small loops form. Such loops are generated by the independent or combined action of mutual friction and reconnection (discussed in the next section). Both mutual friction and reconnection shorten vortex line length and thereby remove rotational kinetic energy from the simulation. Since small loops have high curvature, they move at high speeds and vanish quickly as the loop diameter approaches the scale of the evacuated core diameter. Their rapid motion imposes

stringent accuracy and stability requirements on simulations, resulting in very small time steps for a process that ultimately influences the flow primarily by dissipating kinetic energy. Removing these loops speeds the dissipation process slightly without otherwise impacting the overall dynamics [37]. Qualitatively, this choice is similar to large-eddy simulation of normal-fluid turbulence, in which the impact of unresolved small eddies is typically modeled by augmenting the physical dissipation.

3.8 Reconnection of Vortex Filaments

When two vortices with opposite vorticity approach each other, each vortex distorts the other and a local instability develops. The two momentarily merge, after which the filaments move away from one another in a configuration equivalent to tearing and cross-pairing the torn ends of the original vortices. By estimating the distance at which the nonlocal induced velocity becomes comparable to the local induced velocity Schwarz [41,42], determine that such vortex reconnection becomes an important factor when filaments approach to within a distance $\Delta \approx 2R/Ln(cR/a_0)$ (R is the local curvature, and c is a constant of order 1). This phenomenon is not reflected in the equation of motion of the vortex filament, so it has to be included separately.

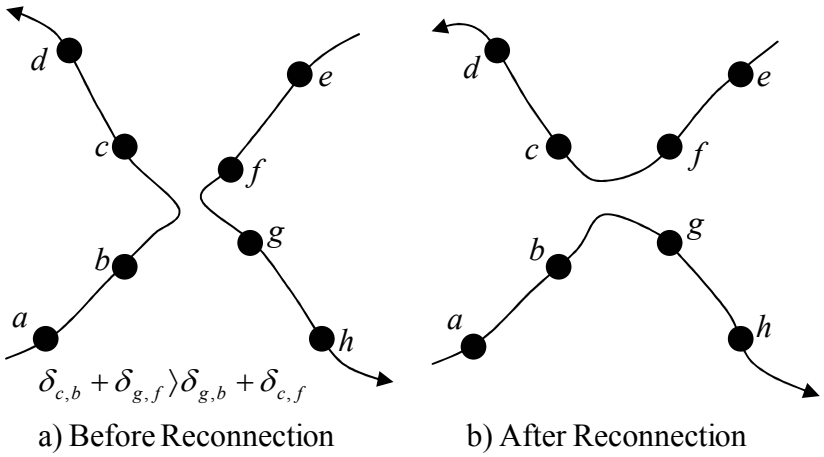

Figure 3.4: Conditions and process of reconnection

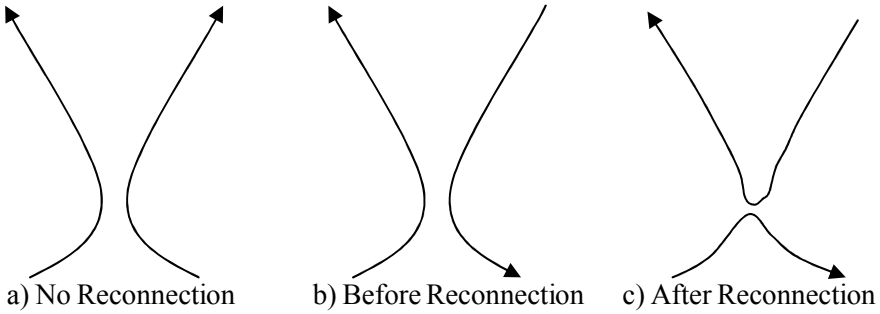

Figure 3.5: Vortex filament reconnection

After the reconnection locations of high curvature that are sometimes formed can generate large amplitude Kelvin waves. These waves play an important role in the development of the superfluid vortex tangle; they are responsible for the transfer of energy from the normal fluid component to the superfluid component that results in the increased tangle density [14,35,36]. It is believed that when superfluid vortex filaments reconnect, mechanical energy is converted to phonons and rotons [37]. The kinetic energy per unit length in a potential flow is given by (3.15) where a is the core radius and b is a characteristic length. This expression relates energy to vortex line length.

$$K = \int_a^b \frac{1}{2}\rho u^2 dr^2 = \frac{\rho\Gamma^2}{4\pi} Ln\left(\frac{b}{a}\right) \tag{3.15}$$

Therefore, two line vortices are allowed to reconnect when doing so results in an overall loss of line length, corresponding to a mechanical energy reduction. Figure 3.4 shows two vortices reconnecting using the line length reduction criterion. As can be seen in Figure 3.5, two vortex filaments reconnect only if they have opposite vorticity. The law of conservation of circulation prevents the reconnection of parallel vortices.

3.9 Boundary Conditions

Since the normal fluid simulation employs periodic boundary conditions (PBC), consistency requires applying the same to the superfluid. PBC for the superfluid are realistic when the line density is high enough to decorrelate the behavior of the distant vortices so the internal dynamics are likely to be statistically independent of the dynamics near boundaries [42]. Assuming PBC implies the simulation box is surrounded by identical boxes extending to infinity. Contributions from the vortex filaments in these boxes must be taken in account when calculating the induced velocity. Although the number of contributions grows cubically with distance, the magnitude of individual contributions decays as the inverse square of the distance from the simulation box. Computational economy dictates truncating the periodic replication of the simulation box close to the box itself. As Figure 3.6 shows, we create an encompassing buffer layer comprising boxes half the size of the simulation box and adjacent to each boundary. The buffer layer allows a softly varying velocity field for vortex filaments that are reentering the periodic domain [37].

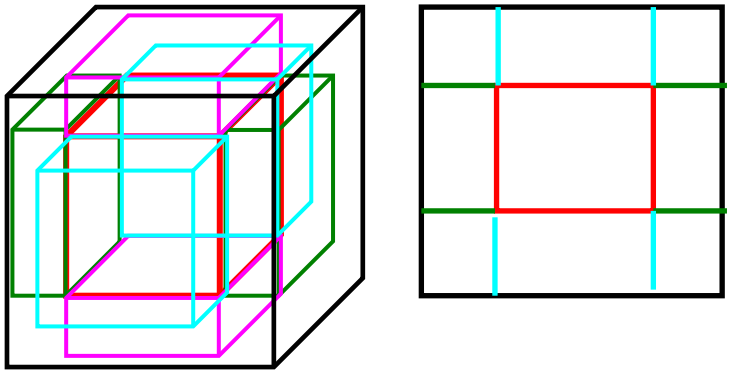

Figure 3.6: Sketch of simulation box and buffer layer to account for images contributions

To implement this approximation, vortex points in the main computational box are translated to the image position as the computation requires. There is no need to save extra points from the images as the vortex filament is advanced in time.

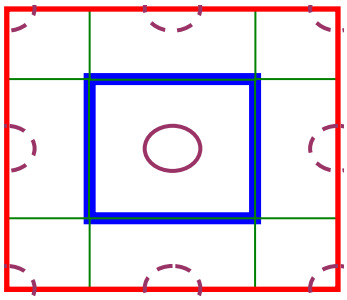

Figure 3.7: Top view of simulation box with a vortex ring and images contributions

Figure 3.7 shows a top view of the computation box, the buffer layer and the image contribution that needs to be taken into account if the vortex filament in the box is a ring. Because of the 2D nature of the figure, images from the top and bottom of the half size boxes are not shown. If the vortex ring is at the center of the box, however, there are no top or bottom contributions regardless since these lie outside the buffer layer.

Chapter 4

Code Verification and Validation

Several tests have been performed to verify that the code implements the above mathematical model correctly and to validate the model itself by comparison to published results, including more fundamental quantum mechanical calculations. In all of our verification and validation simulations, we set $\alpha' = 0$ in equation (2.4). This is valid for temperatures not too close to T_λ since $\alpha' << \alpha$ in this range, although the associated terms in (2.4) are mutually orthogonal and have different effects on the motion of the vortex filament. By contrast, the case studies presented in Sections 4.5 and 4.6, and in Chapter 5 and Chapter 6 include all terms in equation (2.4). A detailed structure of the superfluid component computer code is provided in Appendix C.

4.1 Verification of Induced Velocity Calculation

In the absence of vortex stretching and mutual friction, the motion of a quantum vortex is formally equivalent to that for a classical potential-flow vortex. We can therefore verify the calculation of the remaining driving term, the induced velocity, by comparison to its theoretical value for a classical vortex ring given by equation (4.1) [7]:

$$\mathbf{v}_i = \frac{\Gamma}{4\pi R}\left[\ln\left(\frac{8R}{a_0}\right) - \frac{1}{2}\right] \tag{4.1}$$

This expression for the velocity of a vortex ring in a classical, inviscid fluid is valid when a_0 is negligible compared to the vortex ring radius R. Choosing values characteristic of those we expect in quantum turbulence, we set $\lambda = 0.2cm$, $a_0 = 1x10^{-8}cm$, and $\Gamma = 9.97x10^{-4}$. As can be seen from Figure 4.1, our code calculates the propagation velocity of a vortex ring within 2% of the theoretical value. This calculation included local and non-local contributions without image vortices.

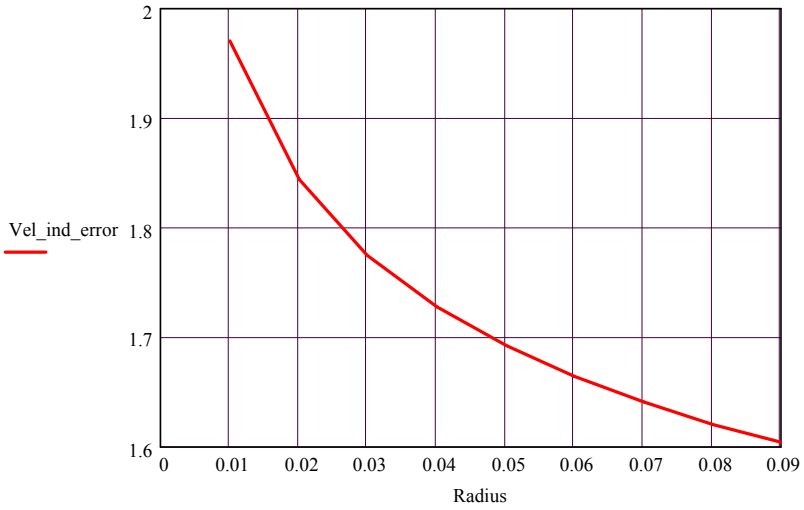

Figure 4.1: Percent error for induced velocity in a single vortex ring for various ring radii in a simulation box of size λ=0.2cm

4.2 Verification of Periodic Boundary Conditions

Verification of the periodic boundary condition implementation involved setting $\mathbf{v}_n = \mathbf{v}_i = \mathbf{0}$ so the vortex moves strictly under the influence of $\mathbf{v}_s$, which we choose to be constant in space and time with only one non-zero vector component. In the absence of remeshing, reconnections and mutual friction ($\alpha = \alpha' = 0$), the ring experiences no deformation. Figure 4.2 shows the vortex ring propagating in a periodic manner in all directions, in agreement with the chosen boundary conditions.

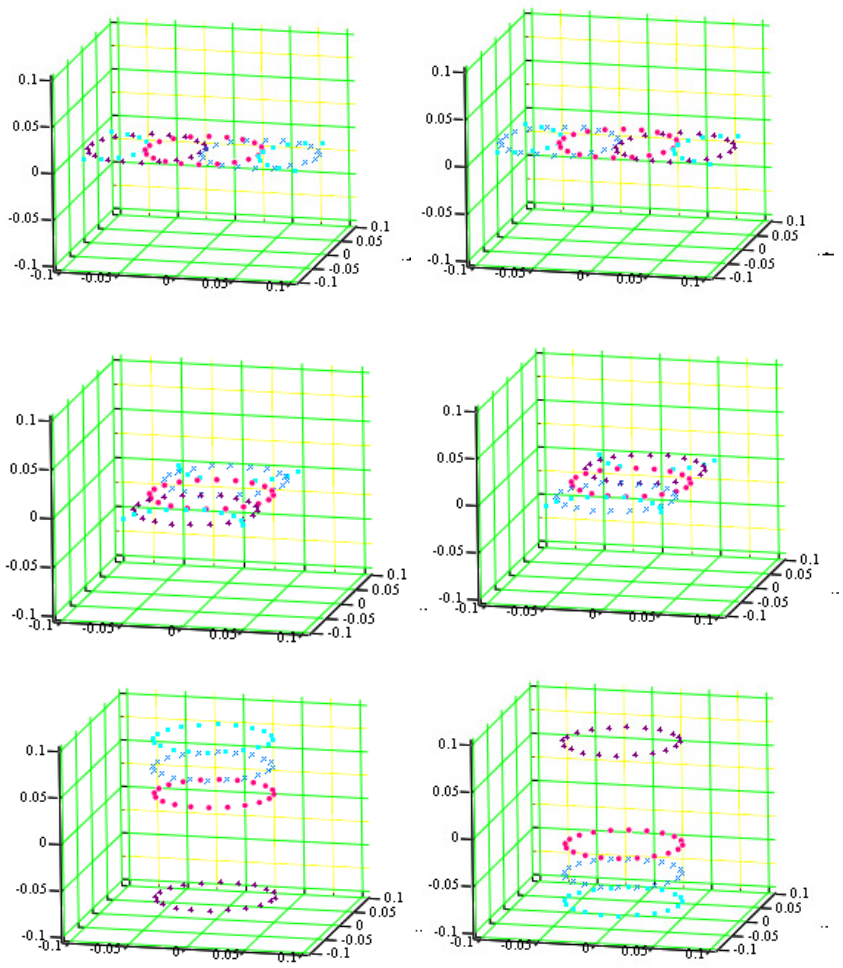

Figure 4.2: Periodic Boundary Conditions enforced in all six directions for a propagating vortex ring
(Colors in increasing time: magenta, blue, cyan, and purple)
(Symbols in increasing time: circles, exes, squares, and crosses)

4.3 Validation of Reconnection Algorithm Implementation

As described in section 3.8, energy arguments suggest that superfluid vortex filaments reconnect if and only if the reconnection results in an overall line length reduction; whereas Kelvin's circulation theorem precludes reconnection of filaments with parallel vorticity. We first verified that these conditions are satisfied by the code and then

validated the conditions themselves by comparison to the more fundamental simulations of Koplik and Levine [17], who employed the nonlinear Schrödinger equation.

The verification tests involved two initially overlapping, coplanar vortex rings. Figure 4.3 shows rings in which the vorticity orientation is counterclockwise as viewed from above the drawing based on the right-hand rule. Because the implied orientation of the vorticity of the connecting segments is opposite, reconnection results in doughnut shaped vortex filament.

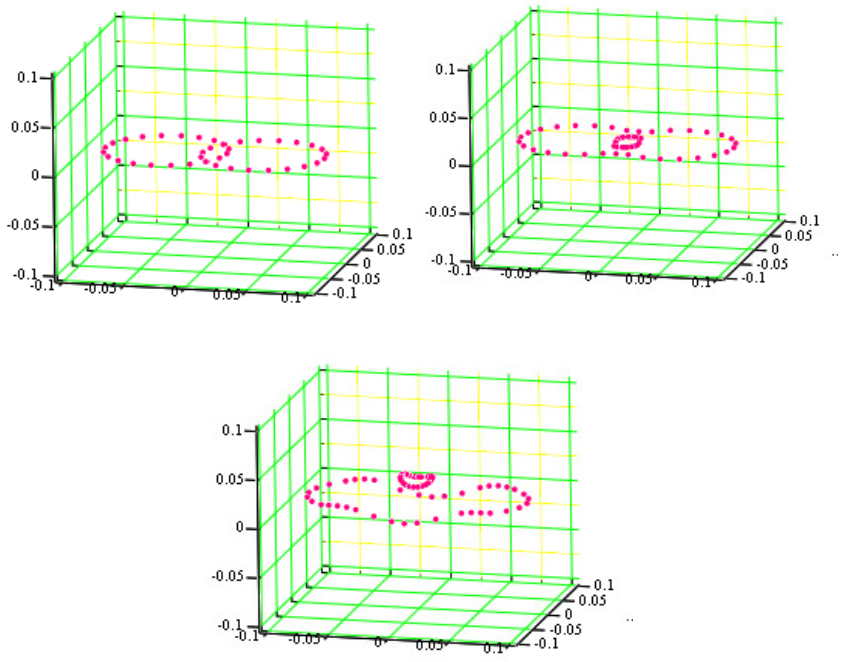

Figure 4.3: Reconnection of vortex rings with counterclockwise vorticity

Figure 4.4 shows two rings with the same geometry as in Figure 4.3, but with different vorticity orientations. The right ring has a clockwise vorticity, while the vorticity of the left ring remains unchanged. The vortices reconnect but remain as two independent rings

that propagate away from each other. The occurrence of reconnection in this case is due to the unrealistic nature of the initial conditions.

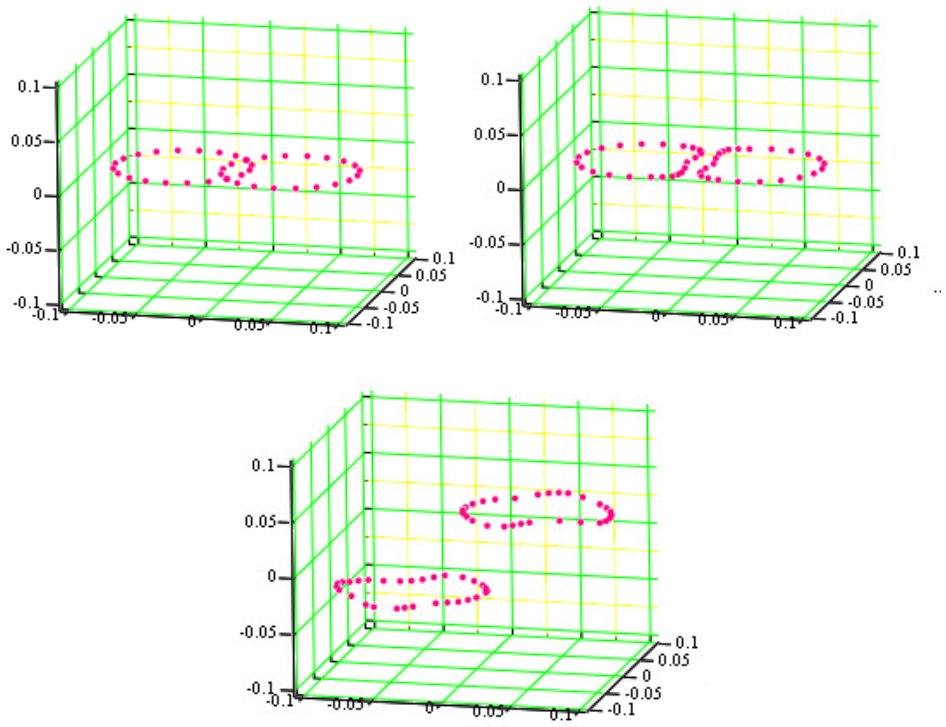

Figure 4.4: Reconnection of two vortex rings with opposite vorticity

To complement the verifications of the expected behavior, validation tests were performed by reproducing the nonlinear Schrodinger calculations published by Koplik and Levine [17]. The vortex filaments are represented by a sinusoidal wave with a mirror image separated by $\lambda/20$. Figure 4.5 through Figure 4.10 demonstrate that our code predicts dynamics in good qualitative agreement with Koplik and Levine. Filaments with anti-parallel vorticity reconnect (Figure 4.5). Those with the same geometry but with parallel vorticity only rotate about each other without reconnecting (Figure 4.7). Finally, orthogonal line vortices separated by $\lambda/20$ reconnect and move apart as time progress (Figure 4.9).

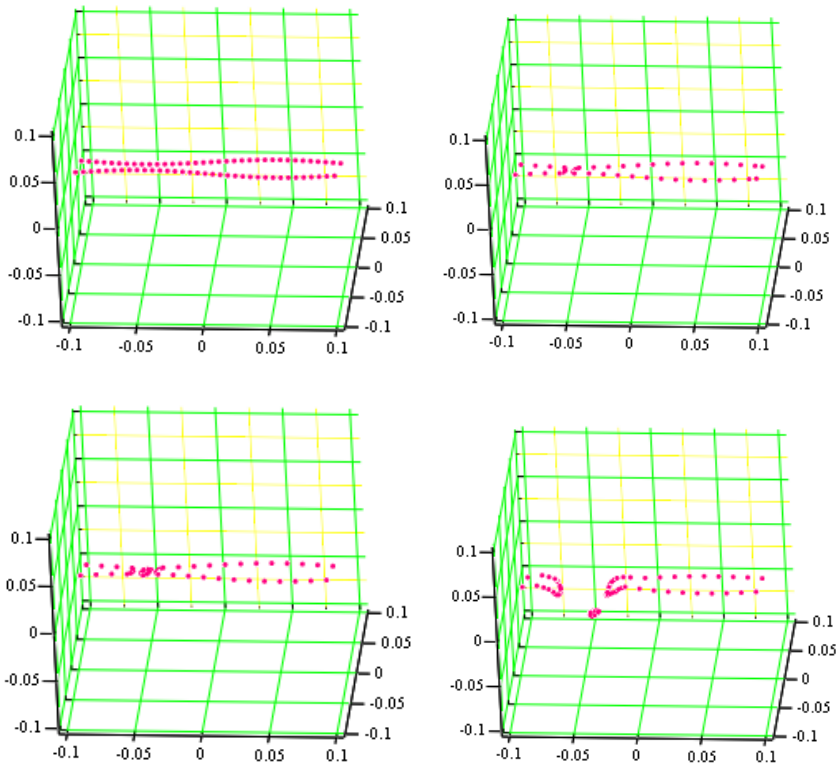

Figure 4.5: Sinusoidal vortex filament with mirror image and opposite vorticity

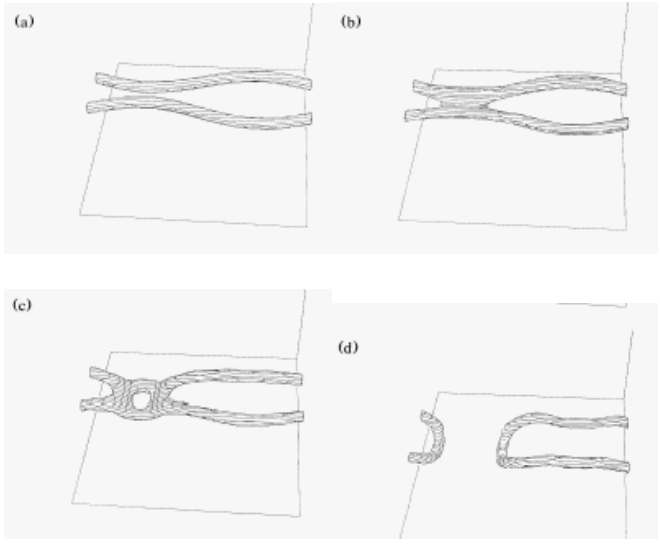

Figure 4.6: Reconnection of antiparallel vortices.
Reprinted with permission from Joel Koplik, Physical Review Letters, 71, 1375 (1993).
Copyright 1993 by The American Physical Society.

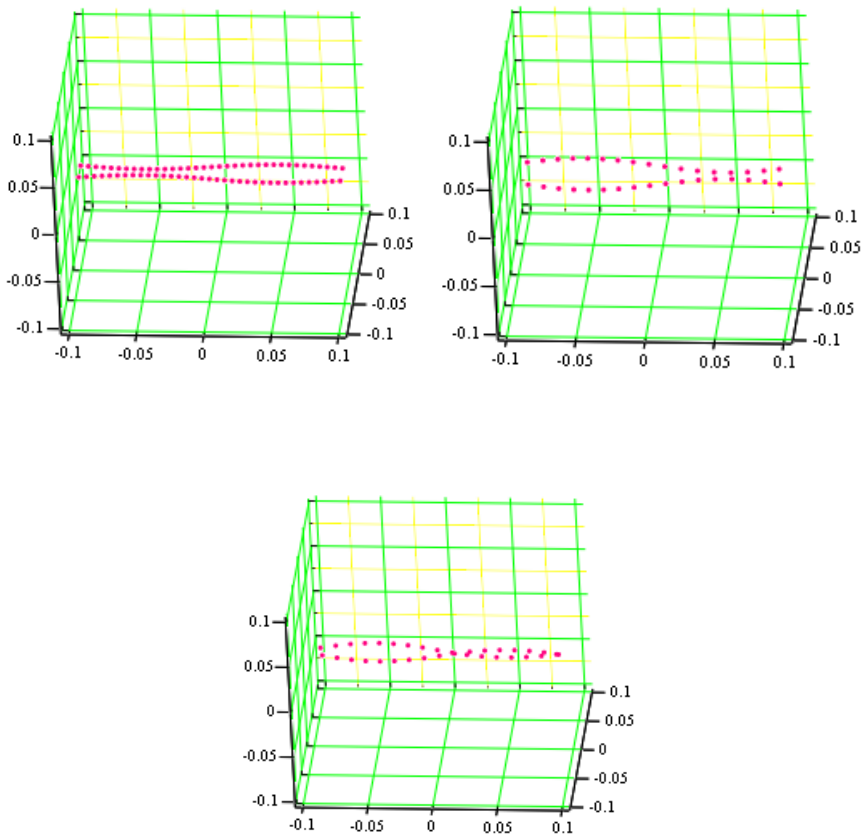

Figure 4.7: Sinusoidal vortex filament with mirror image and parallel vorticity

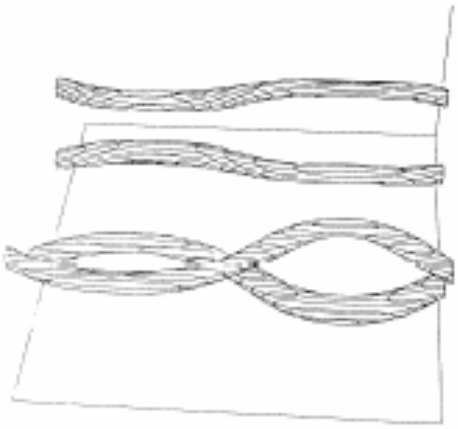

Figure 4.8: Reconnection avoided by parallel vortices.
Reprinted with permission from Joel Koplik, Physical Review Letters, 71, 1375 (1993).
Copyright 1993 by The American Physical Society.

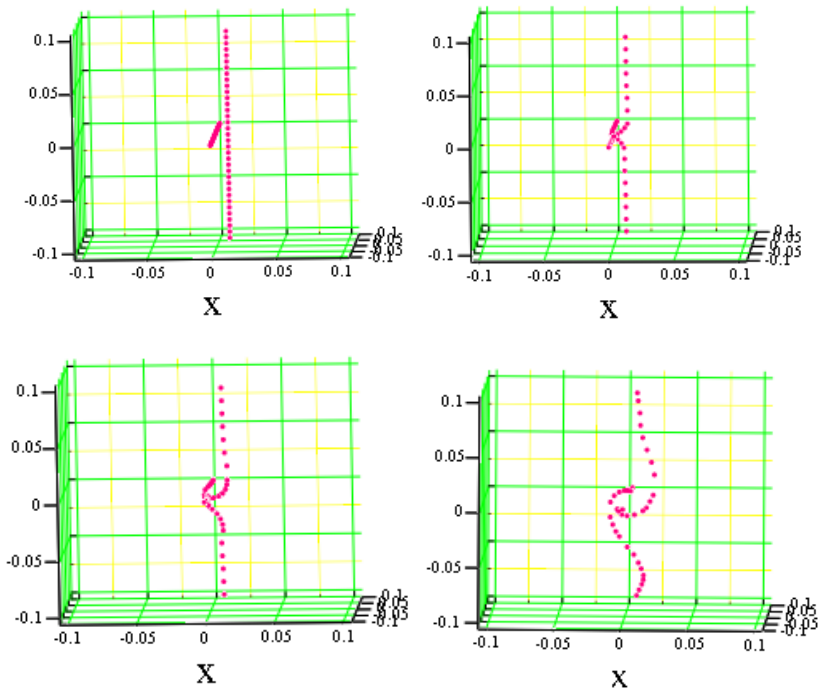

Figure 4.9: Reconnection of orthogonal vortex lines

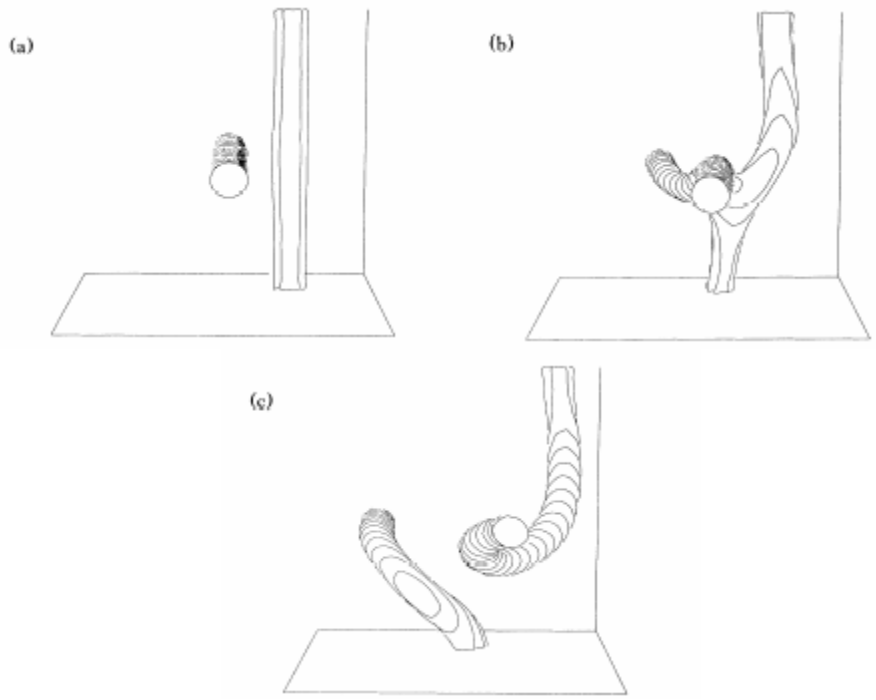

Figure 4.10: Reconnection of orthogonal vortices.
Reprinted with permission from Joel Koplik, Physical Review Letters, 71, 1375 (1993).
Copyright 1993 by The American Physical Society.

4.4 A superfluid vortex driven by ABC normal fluid flow

Barenghi et al. [4] simulated the motion of quantum vortices driven by a steady normal fluid velocity field prescribed by the Arnold-Beltrami-Childress (ABC) conditions:

$$\begin{aligned} v_n^x &= A\sin(2\pi z/\lambda) + C\cos(2\pi y/\lambda) \\ v_n^y &= B\sin(2\pi x/\lambda) + A\cos(2\pi z/\lambda) \\ v_n^z &= C\sin(2\pi y/\lambda) + B\cos(2\pi x/\lambda) \end{aligned} \tag{4.2}$$

which represent a periodic array of vortical motions with varying orientation. Although greatly simplified relative to the broad range of length and time scales in a turbulent flow, the ABC flow draws some inspiration from visualizations of experiments in turbulent water by Schwarz [43]. During the experiment, small scale structures, that were later shown to be regions of concentrated vorticity, were observed. In computer simulations of classical turbulence, these regions manifest as spontaneous appearances of extended vortex tubes with finite length moving perpendicular to their axes [4]. Figure 4.11 and Figure 4.12 shows that our code closely reproduces the Barenghi et al. results at short times. At longer times, Barenghi et al. observed quantum vortex clustering in regions of high normal fluid vorticity. Whether similar results obtain for a more realistic and dynamic turbulent flow field forms one of the central questions addressed in the current project.

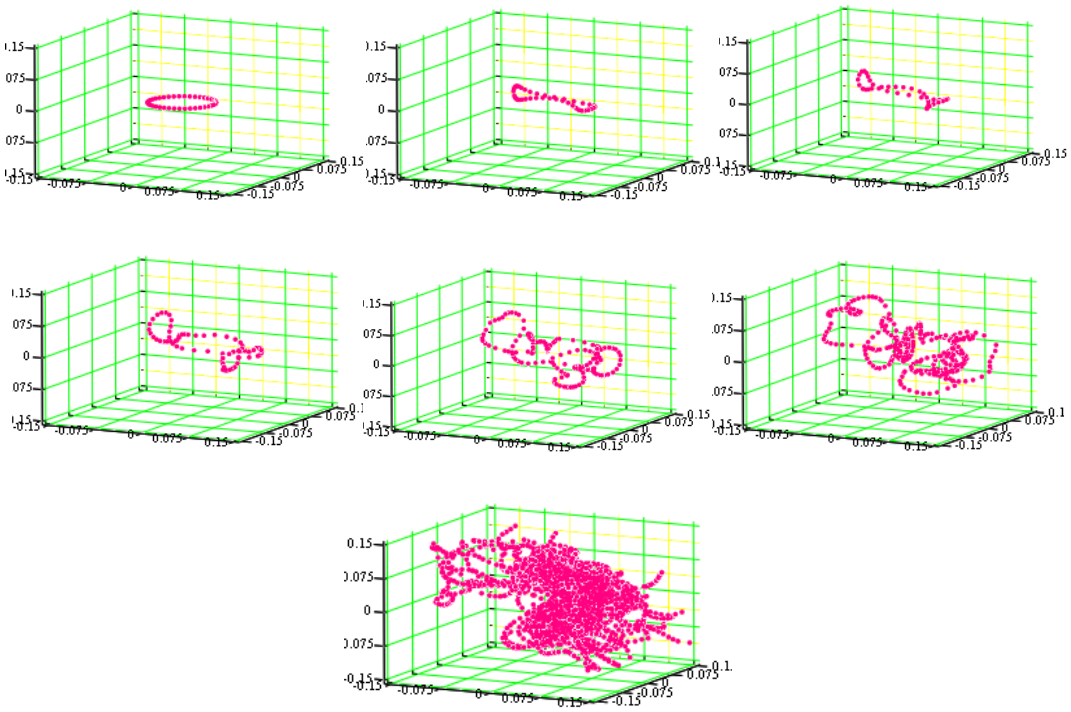

Figure 4.11: Vortex ring in a normal fluid ABC flow with no periodic boundary conditions.

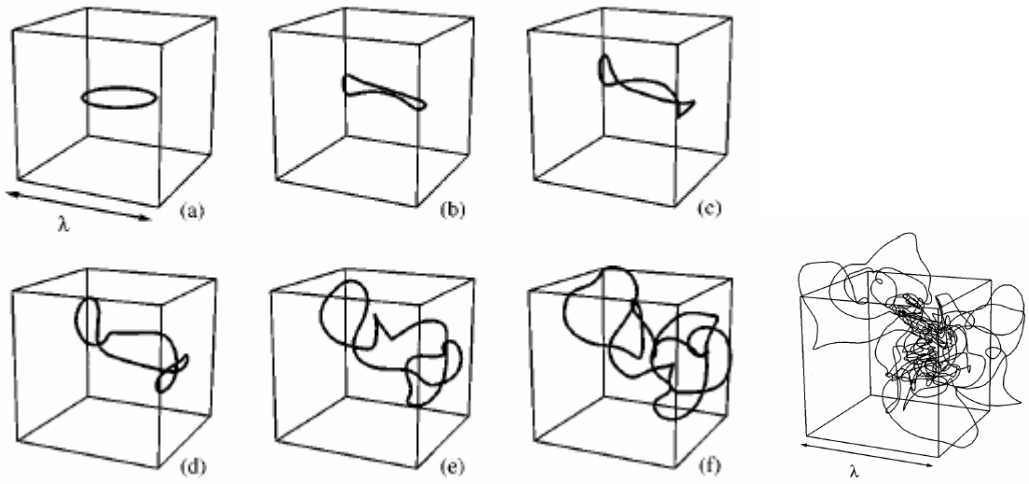

Figure 4.12: Vortex ring in normal ABC flow with no periodic boundary condition.
Reprinted with permission from Carlo F. Barenghi,Physics of Fluids, 9, 2631 (1997).
Copyright 1997, American Institute of Physics.

4.5 Steady Two-Dimensional Taylor-Green Flow

This section and the next present tests inspired by the ABC flow simulations of Barenghi et. al. [4] and other similar work. This type of simulation is limited to the special case of a superfluid in the presence of a steady normal fluid flow. Kivotides et al. [16], for example, utilized a snapshot of a statistically isotropic turbulent flow for the normal fluid component.

We performed several simulations using a symmetric normal fluid field that admits various symmetries. In these tests, the normal fluid was modeled as a 2 dimensional Taylor-Green flow of the form $\mathbf{u}_n = \sin(z)\cos(x)\mathbf{i} + 0\mathbf{j} - \sin(x)\cos(z)\mathbf{k}$. As can be seen from Figure 4.13 this velocity field represents a period array of vortices centered along (-π,y,-π), (0,y,- π), (π,y,-π), (-π,y,0), (0,y,0), (π,y,0), (-π,y,π), (0,y, π), and (π,y,π). The adjacent vortices with opposite circulation generate stagnation points at $\left(-\frac{\pi}{2}, y, -\frac{\pi}{2}\right), \left(\frac{\pi}{2}, y, -\frac{\pi}{2}\right), \left(-\frac{\pi}{2}, y, \frac{\pi}{2}\right), \left(\frac{\pi}{2}, y, \frac{\pi}{2}\right)$.

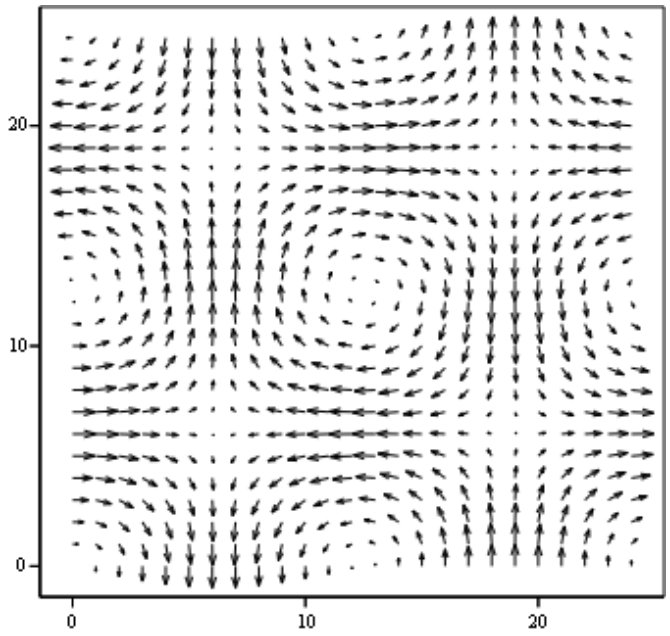

Figure 4.13: Velocity vector field for 2D Taylor-Green flow in a computational grid [-π,π)

The first test consisted of aligning the initial superfluid vortex filaments with the normal fluid Taylor-Green vortex axes of symmetry. We expect the superfluid vortex lines to maintain their initial location because of the zero normal fluid velocity at that location and the fact that discrete, straight-line vortices induced no velocity on themselves. The simulation results agree with our expectations. Another test consisted of 4 superfluid vortex lines aligned along the stagnation regions of the flow. As can be seen in Figure 4.14 the line vortices migrate to the center of the Taylor-Green vortices, indicating that the stagnation lines between normal fluid vortices represent unstable equilibrium points; whereas the stagnation lines at the center of normal fluid vortices represent stable equilibrium points.

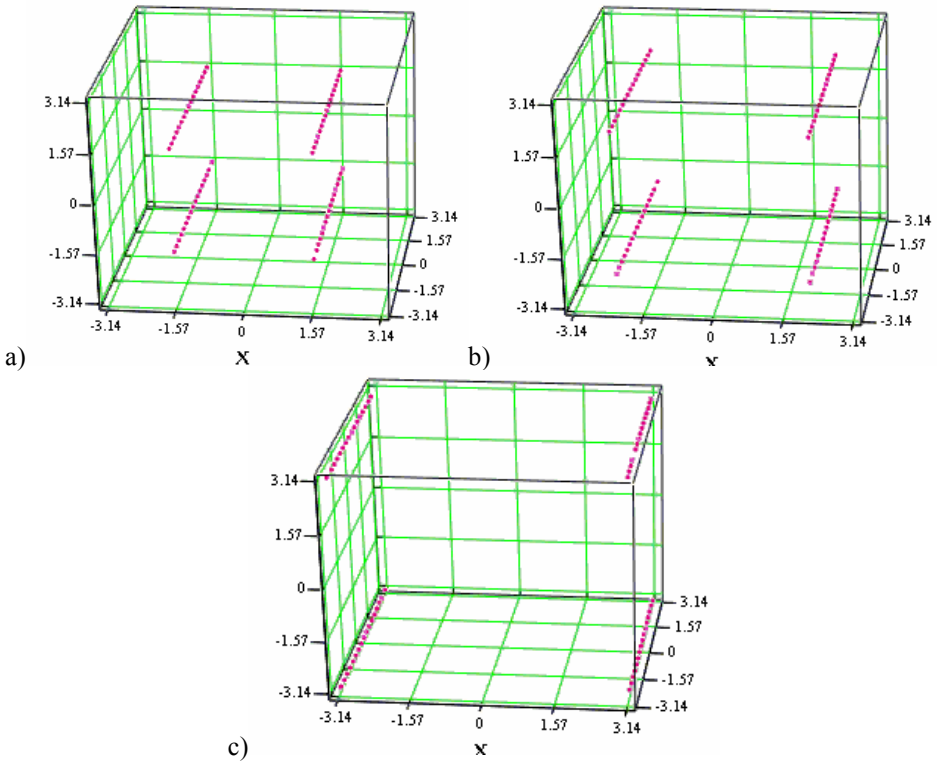

Figure 4.14: Evolution of 4 superfluid vortex filaments in fixed 2D Taylor-Green flow $t_a<t_b<t_c$

The same outcome was observed when the initial configuration included 8 superfluid vortices located at the stagnation lines between Taylor-Green vortices and those at the vortex cores (see Figure 4.15).

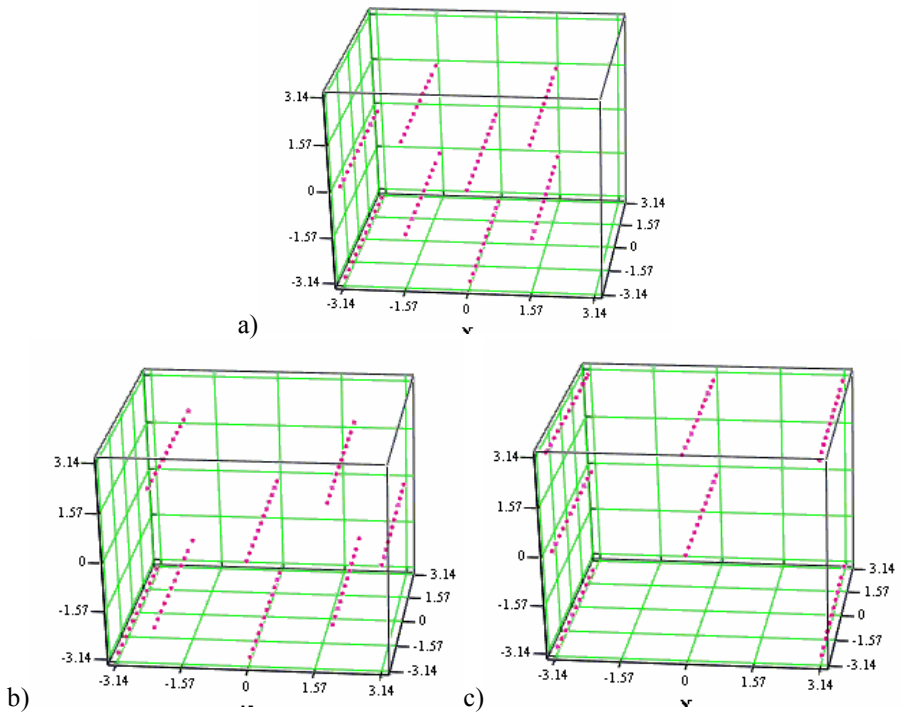

Figure 4.15: Evolution of 8 superfluid vortex filaments in fixed 2D Taylor-Green flow $t_a<t_b<t_c$

The next configuration considered consisted of a single superfluid vortex filament with a slight perturbation, located at the center of the Taylor-Green vortex. As can be seen in Figure 4.16, even in the presence of a perturbation, the filament relocates to the previously observed equilibrium location.

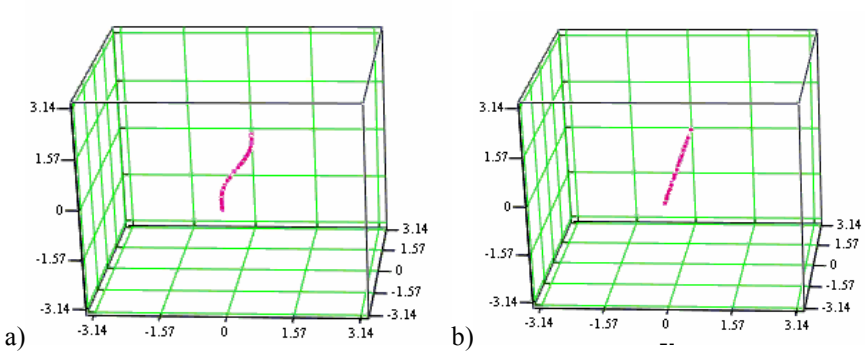

Figure 4.16: Evolution of a single slightly perturbed superfluid vortex filament in fixed 2D Taylor-Green flow $t_a<t_b$

In the final verification simulation for the 2D Taylor-Green flow, the superfluid initial condition comprised 10 rings (see Figure 4.17). Figure 4.18 shows the configuration of the superfluid vortex filament at a later time were the vortex filaments align with the normal fluid vorticity

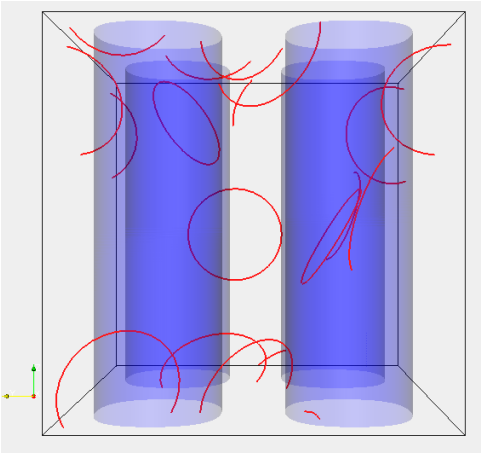

Figure 4.17: Initial condition for fixed 2D Taylor-Green flow in HeII.
Superfluid vortex filaments are shown in red and the normal fluid vorticity isosurface is show in blue.

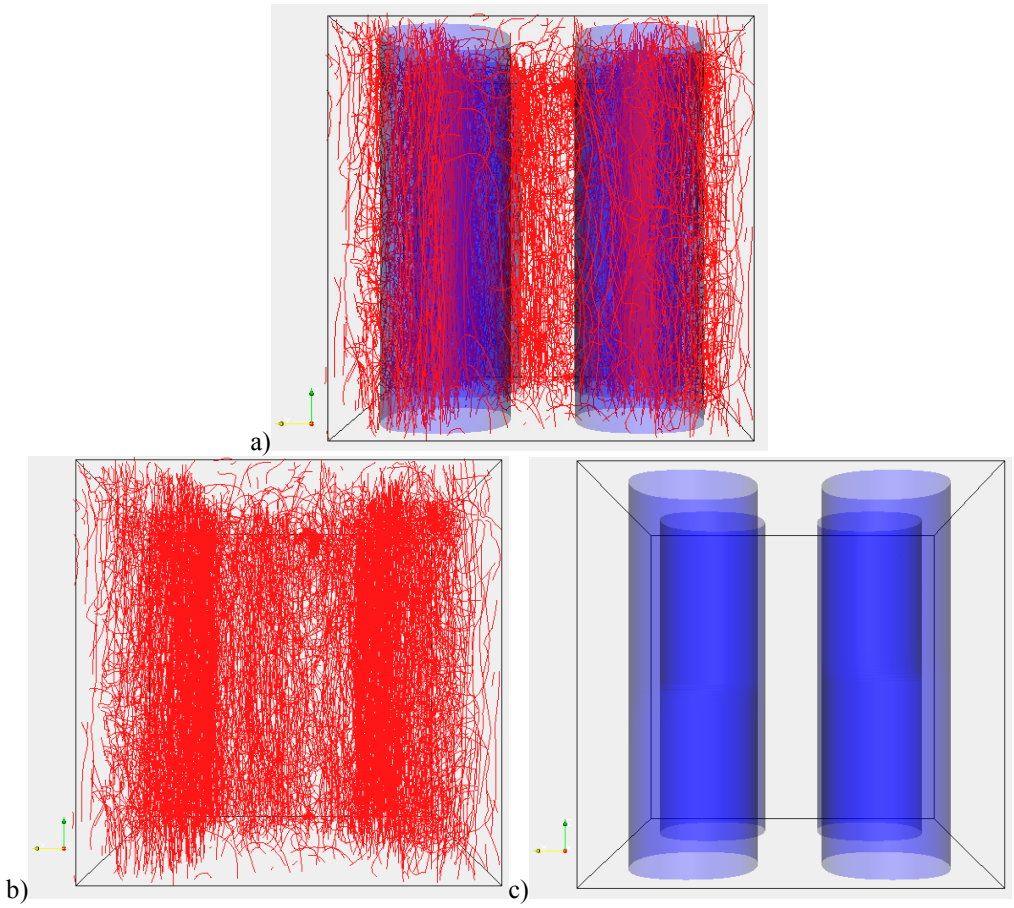

Figure 4.18: Fixed 2D Taylor-Green flow for He II at T=2.1K. a) Superfluid vortex filaments and normal fluid vorticity isosurface. b) Superfluid vortex filaments. c) Normal fluid vorticity isosurface.

4.6 Superfluid vortices driven by a frozen snapshot of a turbulent normal fluid

In this case the normal fluid component is represented by an instantaneous snapshot of a statistically isotropic turbulent field [26]. The chosen fluid properties match He II at a temperature of 2.1K. For the normal fluid component we used a grid size of 64^3. The Taylor microscale Reynolds number is $\mathrm{Re}_\lambda = 18$ and the dimensionless viscosity is ν^*=0.01189. The initial condition for the superfluid component is a vortex filament shaped as 10 random rings (see Figure 4.19). In the presence of mutual friction and

vortex wave instabilities, the flow evolved into a vortex tangle with a higher filament density and a configuration exhibiting a clear alignment of the superfluid vortex filaments along the normal fluid vortices. Results of the flow at t=9.91s are shown in Figure 4.20 where we can visually verify the alignment of the superfluid filaments with the normal fluid vorticity.

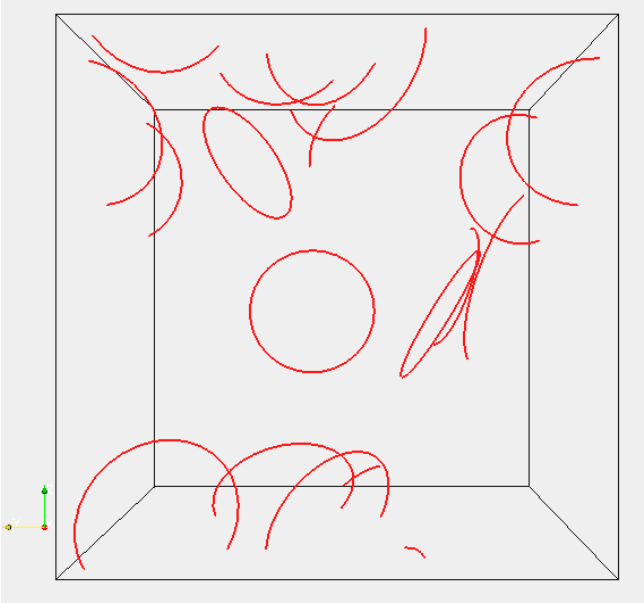

Figure 4.19: Initial condition for superfluid vortex filaments in HeII.

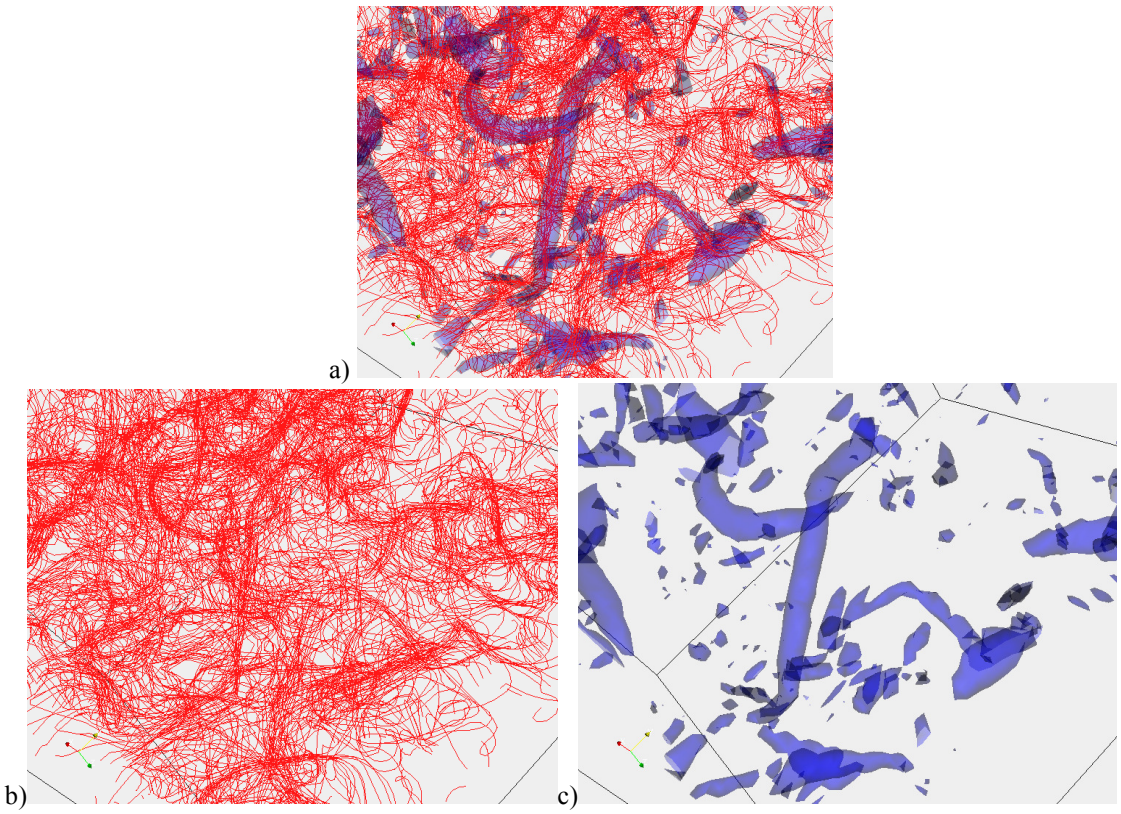

Figure 4.20: Fixed turbulent flow in He^4 at a temperature of 2.1K at t=9.91 s .a) superfluid vortex filaments and normal fluid vorticity isosurfaces b) superfluid vortex filaments c) normal fluid vorticity isosurface.

To quantify the relationship between the vorticity fields we calculated a correlation coefficient for the average vorticity of the two fluid components. The details of the calculation are described in Appendix A and B. Figure 4.21 shows the evolution over time of the correlation coefficient. In agreement with results previously found for superfluid flows with a fixed normal fluid field, the correlation increases over time. On the other hand, we are also able to show that this correlation is stronger for statistics taken over length scales larger compared to the inner vortex line spacing. While the literature contains numerous speculations that the volume-averaged superfluid vorticity behaves classically at larger length scales but differently at smaller length scales, quantitative demonstrations of this length-scale dependency have been missing until now.

Chapter 5 and 6 provide further evidence for this hypothesis in flows of greater complexity than those considered in the current chapter and elsewhere in the literature.

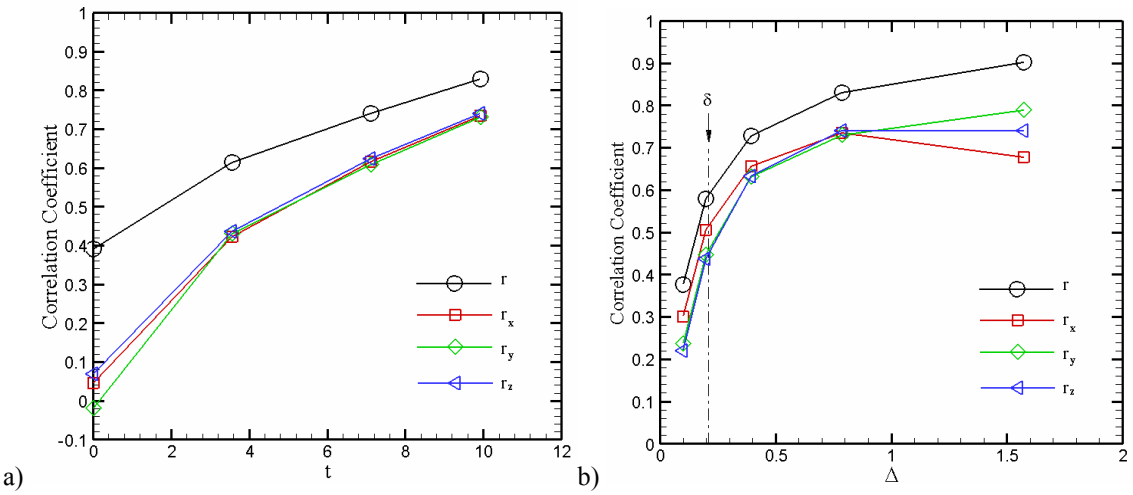

Figure 4.21: Vorticity correlations for a fixed turbulent flow field in He^4 at 2.1K. a) Time evolution of the correlation coefficients of superfluid and normal fluid vorticity; r is the correlation coefficient for the vorticity magnitude and $r_{x,y,z}$ are the coefficients for individual vector components. The vorticity is computed for a cell size Δ=0.785. b) Length scale dependence of the correlation coefficients in a fixed turbulent flow field (t=9.91s): Δ is the cell size and δ is the average inter-vortex spacing (Δ and δ are given relative to the simulation box size)

Chapter 5

Taylor-Green flow with no forcing

5.1 Taylor-Green flow with no forcing in He^4 at T=2.1K

The case considered here involves an evolving Taylor-Green flow with no forcing, so the flow dies out over time. During an intermediate interval within this process, the flow attains a quasi-stationary state characterized by a nearly constant Taylor microscale Reynolds number. In classical turbulence, the Taylor-Green flow has been used previously to study the generation of small length and time scales from large ones [5,48]. In the case of superfluids, numerical experiments on decaying superfluid turbulence of a Taylor-Green flow in He^4 at temperature close to T=0K have found the existence of an inertial range comparable to the Kolmogorov's scaling. At such a low temperature, the normal fluid component is negligible, so pure superfluid flow was studied via the Gross-Pitaevskii equation [25]. In the current case, the DNS was carried out at a temperature of T=2.1K with the following fluid properties: quantum of circulation $\Gamma = 9.97 \times 10^{-4} cm^2/s$, core radius $a_0 = 10^{-8} cm$, $\alpha = 0.498$, $\alpha' = -0.030$, and $\rho_n/\rho = 0.749$ where ρ_n is the density of the normal fluid component and ρ is the density of He II at the working temperature [7,50]. The DNS of the normal fluid component is performed on a grid of 256^3 points, and the initial condition took the form

$\mathbf{u}_n = \sin(x)\cos(y)\cos(z)\mathbf{i} - \cos(x)\sin(y)\cos(z)\mathbf{j} + 0\mathbf{k}$. The initial configuration for the

superfluid component is a collection of 10 identical rings randomly-oriented, with a radius of 0.159cm. Figure 5.1 shows results at the end of the aforementioned quasi-stationary period at t=24.1 s, depicting the obvious visual similarity between the superfluid and normal fluid vorticity.

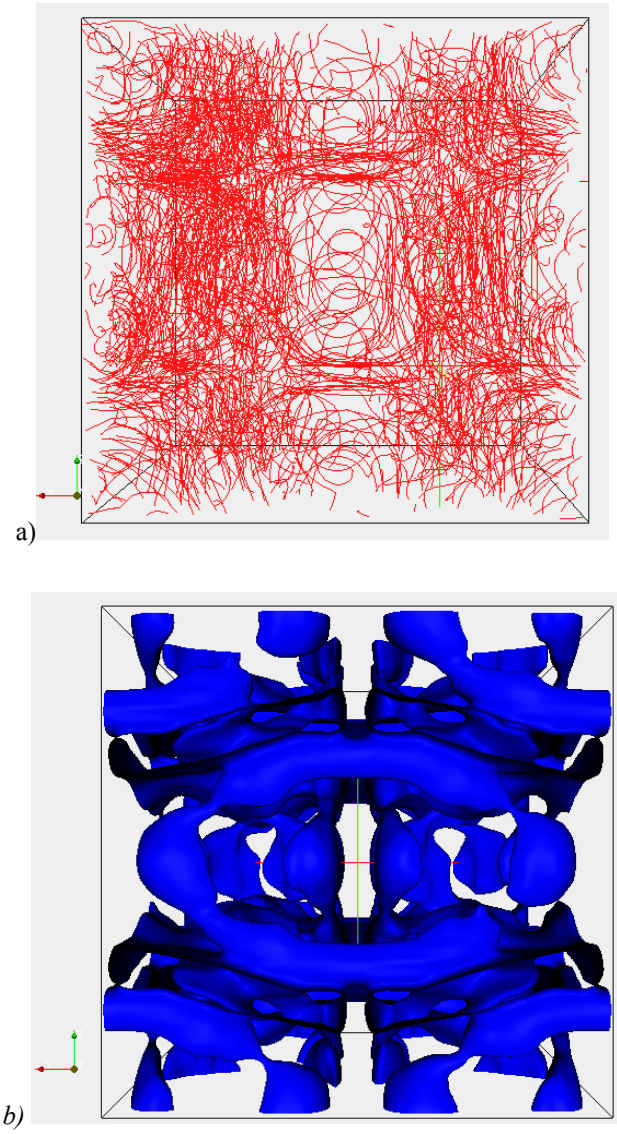

Figure 5.1: Vorticity plots of Taylor-Green flow for He II at T=2.1K, and t=24.1s. a) Superfluid vortex filaments. b) Normal fluid vorticity isosurface.

To quantify the relationship between the two components and assess the degree of vortex locking, we define a vorticity correlation coefficient for the normal fluid and superfluid components as

$$r = \frac{\langle \mathrm{w}_s \mathrm{w}_n \rangle}{\sqrt{\langle \mathrm{w}_s{}^2 \rangle \langle \mathrm{w}_n{}^2 \rangle}} \tag{5.1}$$

where w_n and w_s are either the magnitudes or individual vector components of the normal fluid and superfluid vorticity, respectively. The computational box which has a size of 1cm in every direction is divided into cells of variable size to compute the correlation coefficient as a spatially-averaged function of length scale. Since the vorticity of the superfluid component is confined to the vortex filaments, the total superfluid vorticity of a cell is calculated by summing the contributions of the filaments within it (see Appendix A). For the normal fluid component, the vorticity field is first de-noised via wavelet transforms to extract the coherent vortex structures [10] (see Appendix B), the total vorticity of the cells is then inserted in (5.1). Figure 5.2a depicts the evolution over time of the correlation coefficient, which shows temporally increasing correlations for both the magnitude and the direction of the vorticity. The growth of the correlations with time indicates that the superfluid filaments become increasingly locked to the normal fluid vorticity. To explore the degree of correlation as a function of length scale we calculate the various correlations r_i for the vorticity (w_n and w_s) within cubic cells of linear size Δ. The analysis was performed at the end of the aforementioned quasi-stationary state, when decay starts at t=24.1s. The results are plotted in Figure 5.2b. We see that the correlations are weak for small cell size but grow roughly as $\sqrt{\Delta}$, and in

particular become quite strong once Δ exceeds the average inter-vortex spacing δ ≈ 0.308. (Given a total vortex line length L and simulation box volume V, we estimate δ as $\delta = \sqrt{V/L}$ and normalize by our reference length ($L_{ref} = \frac{1}{2\pi} cm$)).

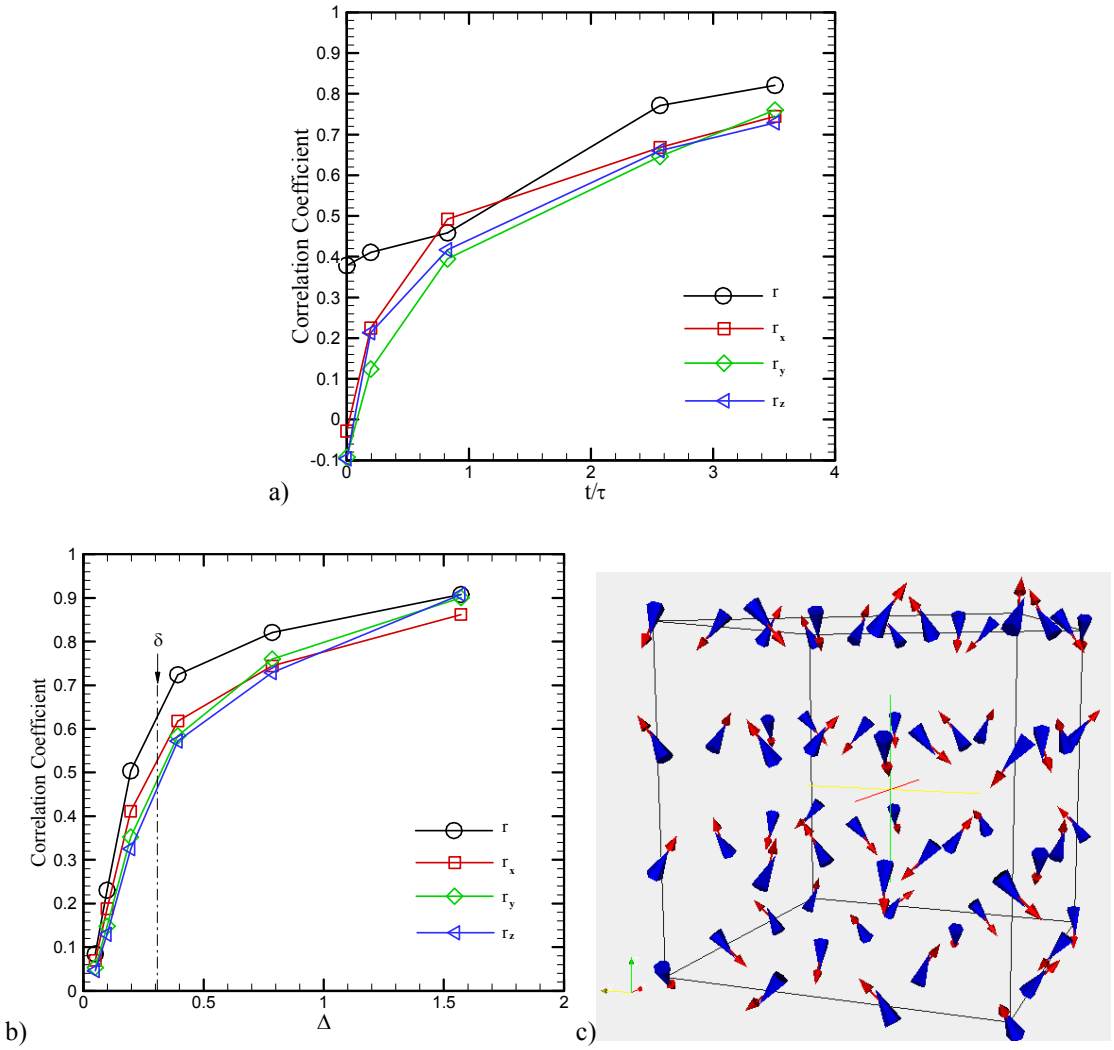

Figure 5.2: Vorticity correlations for the Taylor-Green flow in He^4 at 2.1K. a) Time evolution of the correlation coefficients of superfluid and normal fluid vorticity; r is the correlation coefficient for the vorticity magnitude and $r_{x,y,z}$ are the coefficients for individual vector components, τ is the eddy turnover time of the normal fluid component. The vorticity is computed for a cell size Δ=0.785. b) Length scale dependence of the correlation coefficients in decaying Taylor-Green flow (t=24.1s): Δ is the cell size and δ is the average inter-vortex spacing (Δ and δ are given relative to the simulation box size). c) Vorticity vectors for superfluid vortex filaments (arrows) and normal fluid (cones) at t=24.1s

Chapter 6

Isotropic turbulence with linear forcing

6.1 Isotropic turbulence with linear forcing in He^4 at T=2.1K

Additional numerical simulations were performed where the normal fluid flow was isotropic turbulence (IT) with linear forcing. Experimentally, isotropic flow is typically realized by passing a channel flow through a grid and observing the statistics in a reference frame moving with the mean flow. Since the resulting flow is non-stationary, it is common in simulations to add a fictitious force that injects sufficient energy to keep the flow from decaying. The forcing scheme employed in this dissertation was proposed by Lundgren [21] based on its similarity with the production term in turbulence with mean shear.

With Lundgren's forcing scheme, the Navier-Stokes equation for the normal fluid flow becomes

$$\frac{\partial \mathbf{v}_n}{\partial t} + \mathbf{v}_n \cdot \nabla \mathbf{v}_n = -\frac{1}{\rho}\nabla P + \nu_n \nabla^2 \mathbf{v}_n + \mathbf{F} \tag{6.1}$$

where $\mathbf{F} = A\mathbf{v}_n \equiv (\varepsilon / 3\mathrm{v}_{rms}^2)\mathbf{v}_n$ is the linear force and is related to the energy dissipation rate $\varepsilon = -\nu_n \left\langle \mathbf{v}_n \cdot \nabla^2 \mathbf{v}_n \right\rangle$ and the rms velocity $\mathrm{v}_{rms}^2 = \left\langle \mathbf{v}_n \cdot \mathbf{v}_n \right\rangle / 3$. In this case, we allow the normal fluid to reach a statistically stationary state before introducing the superfluid

component. The superfluid initial configuration is the same as in the Taylor-Green flow – a random collection of vortex rings.

Temperature (K)	1.5	2.1	Reference
ν^*	4.491×10^{-3}	4.491×10^{-3}	[30]
ν_n/Γ	0.843	0.170	[50]
ρ_n/ρ	0.114	0.749	[50]
ρ_s/ρ	0.886	0.251	[50]
α	0.074	0.498	[7]
α'	0.018	-0.030	[7]
Γ (cm^2/s)	9.97×10^{-4}	9.97×10^{-4}	
$\nu_n/\nu^* L_{ref} = u_{ref}$ (cm/s)	1.176	0.237	
A	0.1333	0.1333	[30]
k_0	2	2	[30]
N	128	128	[30]

Table 6.1: Fluid properties and other simulations parameters for isotropic and homogeneous turbulence with linear forcing in He^4

A summary of fluid properties and other important simulation parameters is presented in Table 6.1. The parameters were chosen to match a classical turbulence simulation by Rosales and Meneveau [30] at a Taylor microscale Reynolds number of 42. The fluid temperature for our simulation was T=2.1K. For the normal fluid, the dimensionless viscosity was $\nu^*=4.491 \times 10^{-3}$ and the forcing coefficient was A=0.1333. The initial vortex line length in this flow is L_0=9.98 cm and during the simulation as the energy of the normal fluid component is transferred to the superfluid component the vortex length grows to L_f=1533 cm

An attempt to directly visualize vortex locking is given in Figure 6.1, which shows a cut through the computational box at t=5.65s. While there is certainly some apparent

similarity in the two figures, because of the high vortex line density and the increased randomness of this flow, vortex locking is not as visually obvious as in the previous case. It is in such cases that a statistical analysis similar to the one performed in the Taylor-Green case becomes critically important.

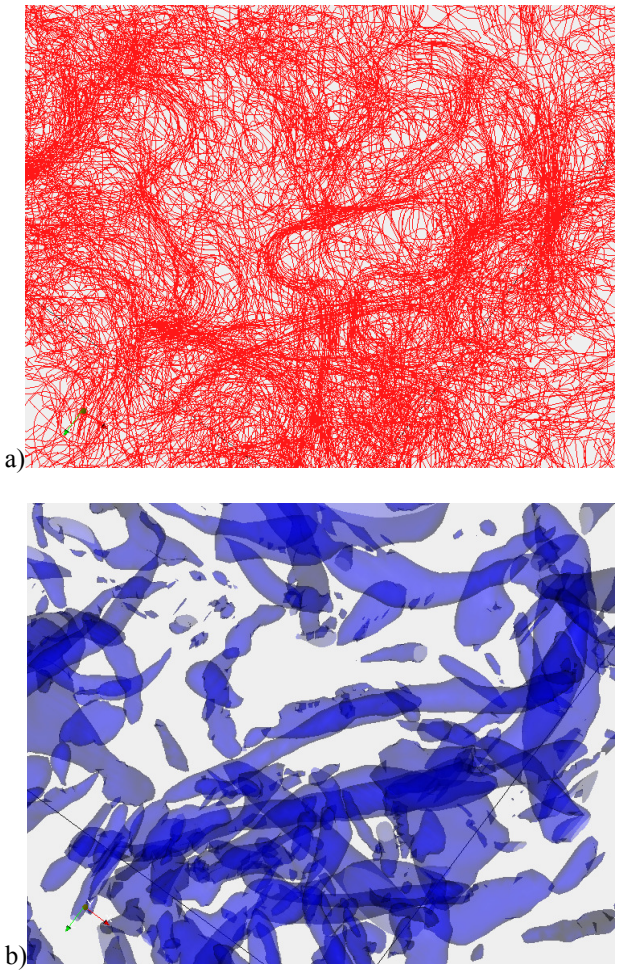

Figure 6.1: Forced homogeneous isotropic turbulence flow in He^4 at a temperature of 2.1K at t=5.65s. a) Superfluid vortex filaments. b) Normal fluid vorticity isosurface.

The time evolution of the correlation coefficients in this case is shown in Figure 6.2a. As before, we find a monotonic increase in the vorticity correlation over time. To analyze our configuration at the final simulated time, we again consider the correlation of

vorticity as a function of cell size Δ. In Figure 6.2b, one can observe large correlations when the vorticity is calculated over length scales larger than the average vortex line spacing. A direct visualization of this correlation in cells of size Δ=1.571 is given in Figure 6.2c, and provides a more local indication of vortex locking.

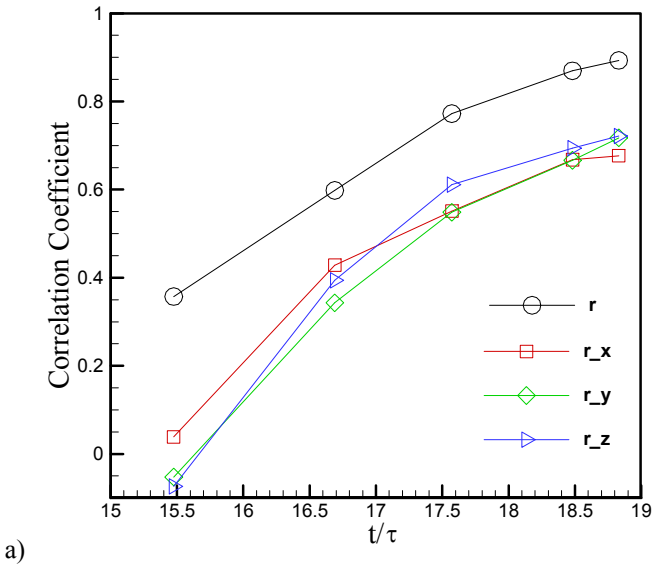

a)

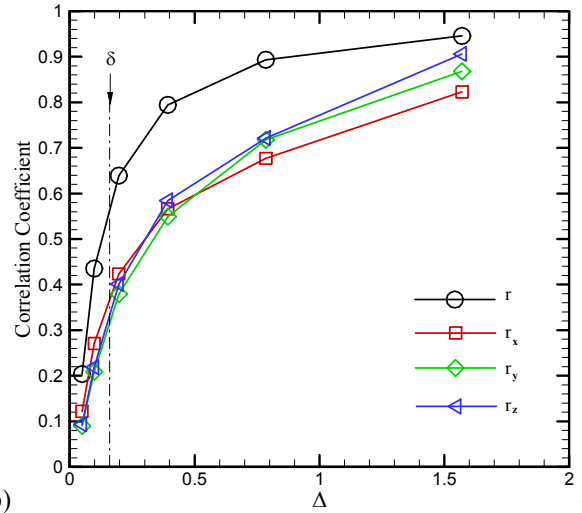

b)

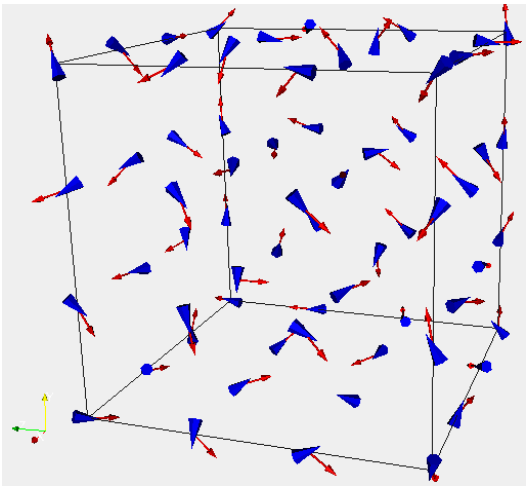

c)

Figure 6.2: Vorticity correlations in forced isotropic turbulence flow in He^4 at a temperature of 2.1K at t=5.65s. a) Time evolution of the correlation coefficients of superfluid and normal fluid vorticity; r is the correlation coefficient for the vorticity magnitude and $r_{x,y,z}$ are the coefficients for individual vector components, τ is the eddy turnover time of the normal fluid component. The vorticity is computed for a cell size Δ=0.785. b) Correlation coefficient of superfluid and normal fluid vorticity as a function of cell size (Δ and δ are given relative to the simulation box size). c) Vorticity vectors for superfluid vortex filaments (arrows) and normal fluid (cones) at t=5.65s.

6.2 Isotropic turbulence with linear forcing in He^4 at T=1.5K

To see how the previous results could be affected by temperature, the simulation was carried out a lower temperature. In this case, there is less normal fluid present: the density ratio is $\rho_n/\rho=0.114$ (11% normal fluid). As a result of the decrease in the normal fluid contribution to the material density, the mutual friction between the two components decreases also. Since the amount of energy being transferred to the superfluid by the normal fluid and the mutual friction are in part responsible for the evolution of the vortex tangle, in this case the tangle that developed was less dense. Figure 6.3 show the vorticity of both superfluid and normal components at t=9.42s, where the alignment of the vorticity is visible in portions of the simulation box.

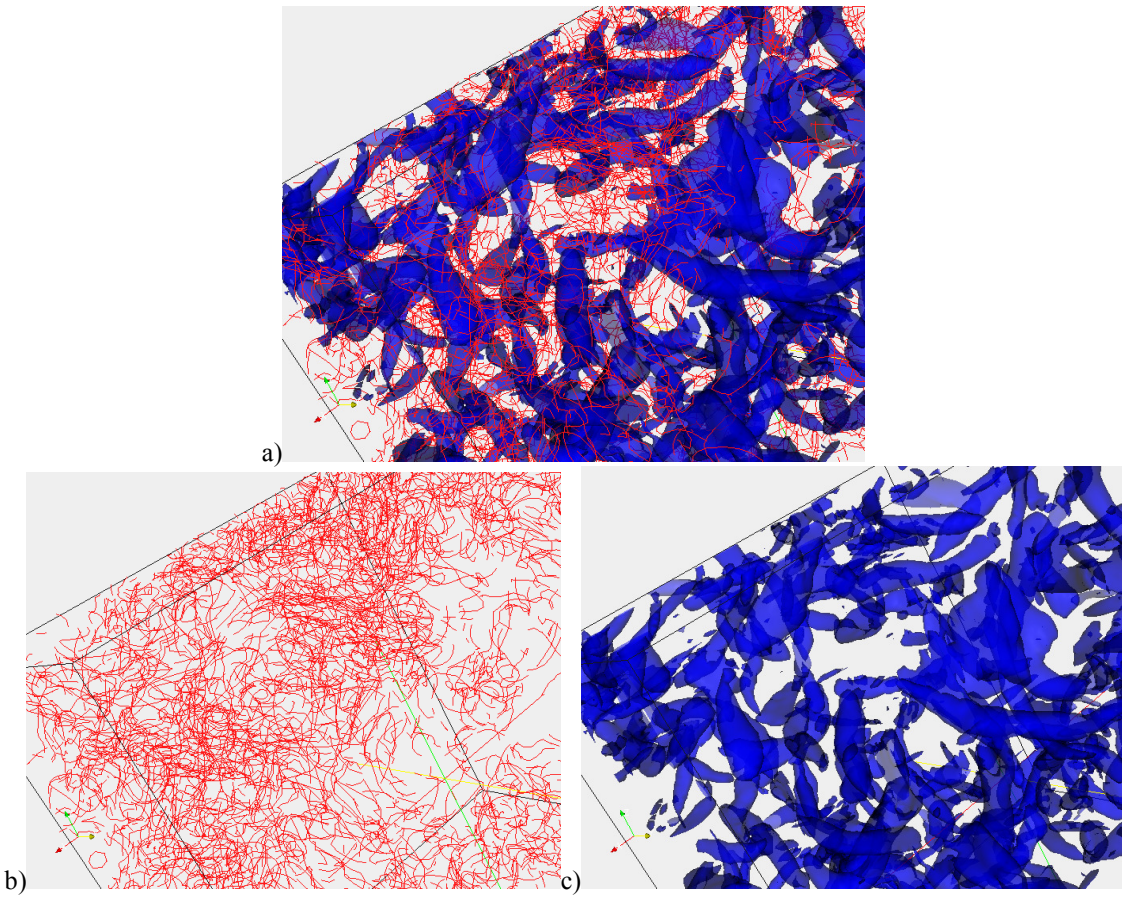

Figure 6.3: Forced homogeneous isotropic turbulent flow in He^4 at a temperature of 1.5K at t=9.42 s .a) superfluid vortex filaments and normal fluid vorticity isosurfaces b) superfluid vortex filaments c) normal fluid vorticity isosurface.

To quantify the relationship of the vorticity, the same data analysis was performed as previously done. As can be seen from Figure 6.4, the correlation increases over time for both the vorticity magnitude and direction, and the correlation is considerably stronger for length scales larger than the inter-vortex spacing. However, in this case, the correlation for the vorticity direction does not increase as fast as the magnitude does. This is likely a direct consequence of the aforementioned decrease in mutual friction attendant to the decreased ratio of normal fluid component density to total density. Since the simulations are one-way coupled, the normal fluid executes the same motion as in the case at T=2.1K, but the vortex line formation is enhanced less.

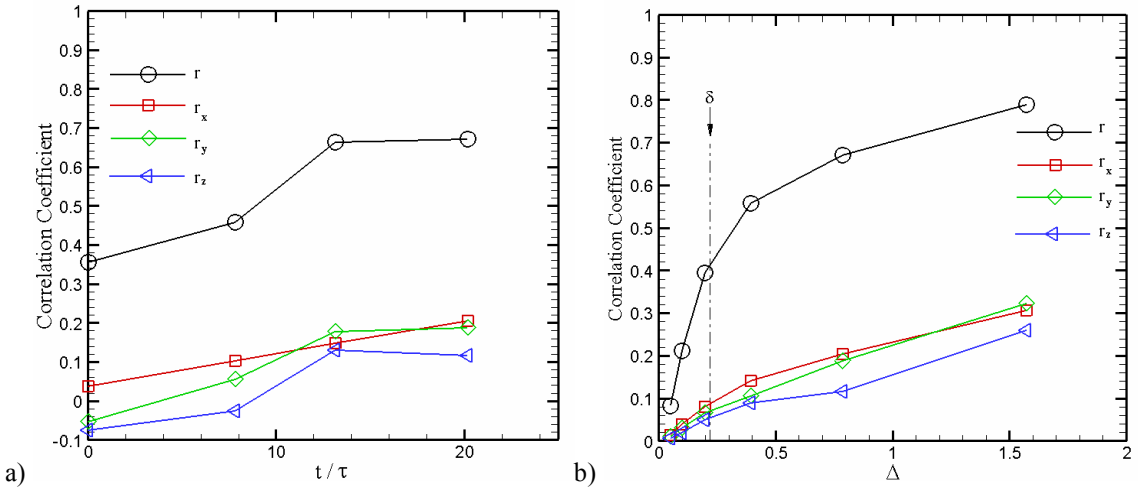

Figure 6.4: Vorticity correlations in forced isotropic turbulence flow in He^4 at a temperature of 1.5K at t=9.42s. a) Time evolution of the correlation coefficients of superfluid and normal fluid vorticity; r is the correlation coefficient for the vorticity magnitude and $r_{x,y,z}$ are the coefficients for individual vector components, τ is the eddy turnover time of the normal fluid component. The vorticity is computed for a cell size Δ=0.785. b) Correlation coefficient of superfluid and normal fluid vorticity as a function of cell size (Δ and δ are given relative to the simulation box size)

Chapter 7

Conclusion

We have presented a description and solution of the mathematical model used to simulate the flow of He II. This model is based on the two-fluid model used to explain the macroscopic properties of He II. According to the two-fluid model, superfluid helium is a mixture of two interpenetrating fluids: a normal fluid and a superfluid component. The normal fluid is modeled using DNS, which means that the NSE is solved directly to generate statistically homogenous isotropic turbulence. The superfluid, on the other hand, is modeled according to the vortex filament method. Each quantized vortex filament is discretized, and the motion of the collection of points is calculated taking into account both local and nonlocal contributions of the induced velocity generated by the vortices. In addition to the induced velocity, the vortices are subject to reconnection. The superfluid component interacts with the normal fluid component through mutual friction. Extensive superfluid code validation and verification tests were performed to ensure reliable results.

By performing a DNS of a turbulent helium flow, we were able to confirm previous conjectures regarding the experimentally observed similarities in the macroscopic statistics of classical and quantum turbulence. In the one-way coupled evolution, the

superfluid component absorbs energy from the normal fluid component, and as a result of mutual friction and vortex wave instabilities, a highly dense vortex tangle develops, wherein the superfluid vortex filaments align with the normal fluid vorticity. Once this alignment, or locking, of quantum vortices and classical vortices has occurred, both components follow a similar motion. This was directly observed for a linearly forced, isotropic turbulent flow where the similarities between superfluid and normal fluid components increased as the flow evolved. These statistical similarities are most pronounced at length scales that are large compared to the inter-vortex spacing.

Future Work

The following step would be to extend the functionality of the present code to account for the back reaction of the superfluid on the normal fluid. A study of isotropic turbulence for both forced and decaying cases will determine the impacts of the approximation made in this work. A fully coupled simulation, will be capable of verifying, by direct calculation, the experimental results obtained for effective eddy viscosity (see Figure 7.1). In this experiment, the dissipation rate of grid turbulence in helium II is derived based on analogies to classical turbulence [47]. The results can in turn be used to increase our understanding of experimental findings that prove the existence of a drag crisis in spheres flowing in He II [6,44].

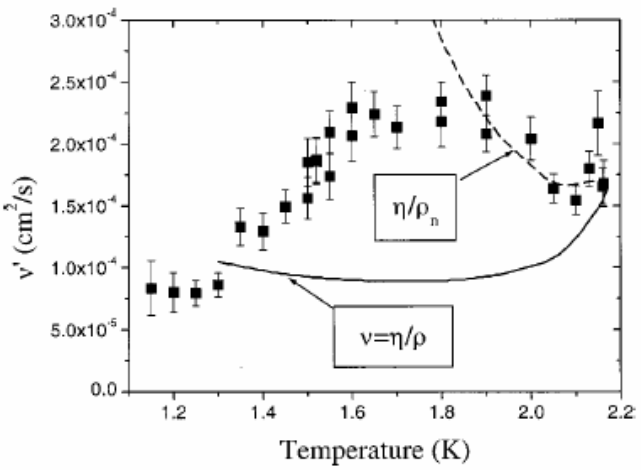

Figure 7.1: Effective kinematic viscosity as a function of temperature measure from experiments. Reprinted with permission from Steven R. Stalp, Physics of Fluids, 14, 1377 (2002). Copyright 2002, American Institute of Physics.

Appendix A: Calculation of Average Superfluid Vorticity

In this calculation the periodic computational box is divided into a series of identical cells. The correlation coefficient for the normal fluid and superfluid vorticity fields is calculated based on the average vorticity of the different cells. Following the two fluid model the superfluid component is a background inviscid, and irrotational flow with floating vortex filaments of constant core radius and quantized circulation. Using the fact that the vorticity of the superfluid component is limited to the interior of these vortex filaments we calculate the average superfluid vorticity within a cell ($\mathbf{w}_s^{avg}$) by integrating for the circulation over all the vortex filaments within that particular cell, and dividing the result by the volume of the cell.

$$\mathbf{w}_s^{avg} = \frac{\sum_{filaments\ in\ cell} \Gamma \Delta \mathbf{s}_{j,j+1}}{\Delta x \Delta y \Delta z}$$

where Δx , Δy ,and Δz are the cells dimensions in all three directions, and they are all equal to Δ , and $\Delta \mathbf{s}_{j,j+1}$ is a vortex point spacing vector. Figure A.1 shows an example for the vortex point spacing vector in a section of a vortex filament inside a cell. Results obtained for $\mathbf{w}_s^{avg}$ are substituted into equation (5.1) to calculate the correlation coefficient.

. a)

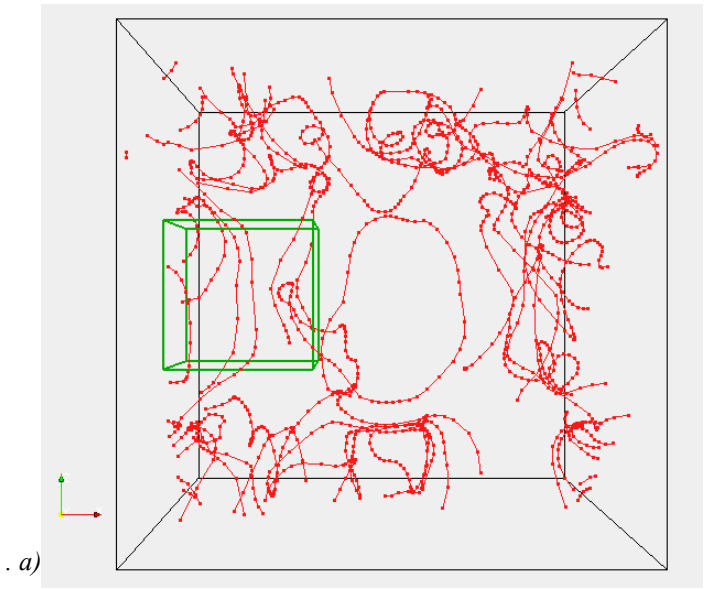

b)

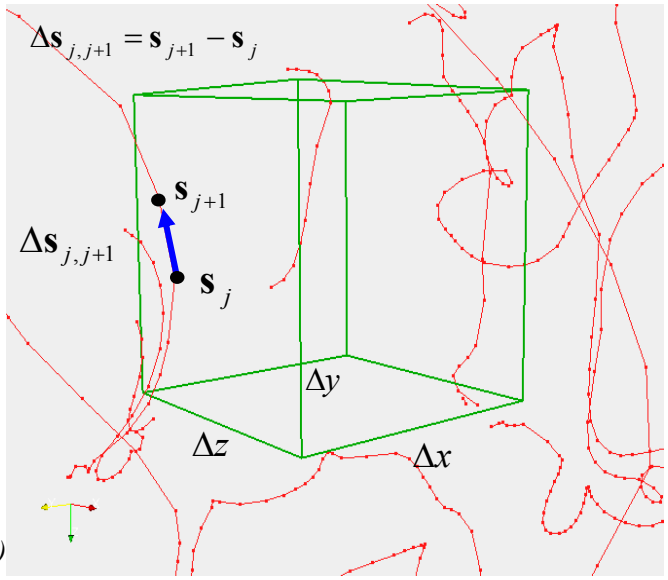

Figure A.1: a) Computational box with superfluid vortex filaments, b) Sample cell with parameters used to calculate vortex filament contribution to average superfluid vorticity.

Appendix B: Denoising of Normal Fluid Vorticity

To identify structures of coherent vorticity the normal fluid vorticity field is denoised by applying a coherent vortex extraction algorithm. The algorithm uses discrete wavelet transforms (DWT) to separate the vorticity field into two orthogonal components: (1) a coherent component with organized structures and (2) an incoherent component that is random and amorphous. All length scales in the inertial regime are represented in both components. However, the statistical behavior of each component is different, and the Kolmogorov spectrum is only a characteristic of the coherent component.

The coherent vortex extraction procedure we followed is similar to the one used by Farge [10]. The first step in the algorithm is to perform three DWT one for each vorticity component. We use a Daubechies 12 wavelet, which has 6 vanishing moments, and 12 wavelet function coefficients. The DWT is done by multiplying the vector data of length N by the transformation matrix, the resulting smooth vector data of length $N/2$ is then multiply again by the transformation matrix. The process is repeated until a vector data of length 2 is obtained, the method is known as a pyramidal algorithm [28]. The second step is to denoised the normal fluid vorticity field by applying a threshold to the wavelet coefficients such that only wavelet coefficients with a magnitude larger that the set threshold are consider. The threshold (T) as defined by Farge [10] is

$$T = \left(\frac{4}{3} Z \log N \right)^{1/2}$$

$$Z = \frac{1}{2} \langle \mathbf{w}, \mathbf{w} \rangle$$

where Z is the normal fluid enstrophy and N is the number of grid points. The threshold expression is related to the characteristic equation for soft thresholding

$T = RMS(2\log N)^{1/2}$ where RMS is the root mean square of the signal, which represents the noise amplitude. The main advantage of denoising by soft thresholding is that we are able to attain a smooth denoised signal [8].

The last step is to recover the coherent vorticity field by performing three inversed discrete wavelet transforms (IDWT) which are obtained by multiplying the thresholded wavelet coefficients by the transpose of transformation matrix following the same pyramidal algorithm. The resulting coherent vorticity field is used in the calculation of the correlation coefficient according to equation (5.1)

Appendix C: Code Structure for Superfluid Component

The superfluid component is modeled and solved using vortex filament methods. Figure C.1 shows an object diagram of the code structure. Each box is split into three parts:

1. The top part of the box specifies the module file name
2. The middle section of the box describes the local data
3. The bottom of the box includes a list of private and publicly accessible procedures.

Private data and procedures are preceded by a minus sign. Public data and procedures are preceded by a plus sign. The procedure return type follows the procedure name and argument list specification. The arrows are used to describe the one direction association between the different objects.

The vortex filaments are represented by a collection of vortex points. Module Vortex_Point.f90 includes a point class that holds the position of a vortex point. The superfluid vortex tangle present in the quantum flow as well as the major physics associated with the tangle including local and nonlocal induced velocity, reconnection and remeshing are dealt with in module Tangle.f90. This module contains a tangle class that keeps track of all vortex points in the simulation as well as the connectivity of these points. The Finite_Difference.f90 module calculates first and second derivatives of $\mathbf{s}$ with respect to the arclength ξ. Global.f90 holds constant parameters and basic operator

functions used by all other modules. The equation of motion is advanced using module Integrator.f90, which is called in Main.f90 the driver of the code.

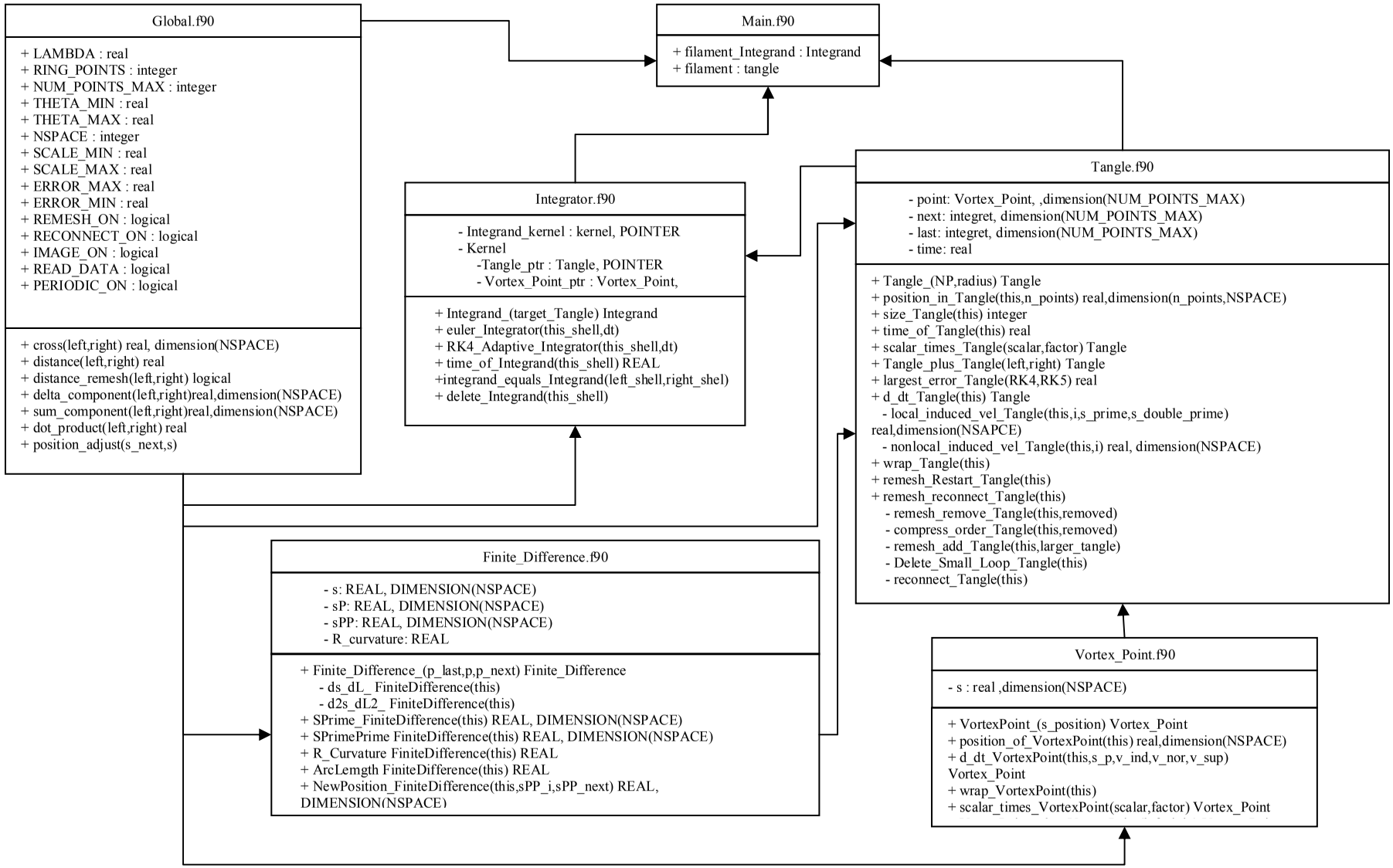

Figure C.1: Object diagram for superfluid component code

References

1. Alexandrou, A., 2001, *Principles of Fluid Mechanics*, 1st edition, Prentice-Hall, INC, Upper Saddle River, NJ.
2. Araki, T., Tsubota, M., and Nemirovskii, S. K., 2002, *Energy Spectrum of Superfluid Turbulence with No Normal-Fluid Component*, Phys. Rev. Lett. **89**(14), pp. 145301(4).
3. Barenghi, C. F., 2001, *Introduction to Superfluid Vortices and Turbulence, in Quantized Vortex Dynamics and Superfluid Turbulence*, Springer, New York.
4. Barenghi, C. F., Samuels, D. C., Bauer, G. H., and Donnelly, R. J., 1997, *Superfluid vortex lines in a model of turbulent flow*, Phys. Fluids, **9**(9), pp. 2631-2643.
5. Brachet, M. E., Meiron, D. I., Orszag, S. A., Nickel, B. G., Morf, R. H. and Frisch, U., J., 1983, *Small Scale Structures of the Taylor-Green Vortex*, J. Fluid Mech., **130**: pp. 411-452.
6. Choi, Y. S., Smith, M. R., and Van Sciver, S. W., in *Quantized Vortex Dynamics and Superfluid Turbulence,* edited by C. F. Barenghi, R. J. Donnelly, and W. F. Vinen, Lectures Notes in Physics (Springer, New York, 2001)
7. Donnelly, R. J., 1991, *Quantized Vortices in Helium II*, Cambridge University Press, New York, NY.
8. Donoho, D. L., 1995, *De-Noising by Soft-Thresholding*, IEEE Trans. Inf. Theory **41**(3), pp. 613-627.
9. Fairbank, H. A. and Lane, C. T., 1949, *Rollin Film Rates in Liquid Helium*, Phys. Rev. **76**(8), pp. 1209-1211.
10. Farge, M., Schneider, K., Pellegrino, G., Wray, A. A., and Rogallo, R. S., 2003, *Coherent vortex extraction in three-dimensional homogeneous turbulence: Comparison between CVS- wavelet and POD-Fourier decompositions,* Phys. Fluids, **15**(10), pp. 2886-2896.
11. *Helium*, In Wikipedia The Free Encyclopedia. Retrieved August 7, 2006, from http://en.wikipedia.org/wiki/Main_Page
12. Idowu, O. C., Kivotides, D., Barenghi, C., and Samuels, D., in *Quantized Vortex Dynamics and Superfluid Turbulence,* edited by C. F. Barenghi, R. J. Donnelly, and W. F. Vinen, Lectures Notes in Physics (Springer, New York, 2001)
13. Kapitza, P., 1938, *Viscosity of Liquid Helium below λ-Point,* Nature, **141**(74).
14. Kivotides, D., Vassilicos, C. J., Samuels, D. C., and Barenghi, C. F., 2001, *Kelvin Waves Cascade in Superfluid Turbulence*, Phys. Rev. Lett., **86**(14), pp. 3080-3083.
15. Kivotides, D., Vassilicos, C. J., Samuels, D. C., and Barenghi, C. F., 2002, *Velocity spectra of Superfluid Turbulence,* Europhys. Lett., **57**(6), pp. 845-851.

16. Kivotides, D., 2006, *Coherent Structure Formation in Turbulent Thermal Superfluids*, Phys. Rev. Lett., **96**(17), pp. 175301(4).

17. Koplik, J. and Levine, H., 1993, *Vortex Reconnection in Superfluid Helium*, Phys. Rev. Lett., **71**(9), pp 1375-1378.

18. Landau, L., 1941, *Theory of Superfluidity in Helium II*, Phys. Rev., **60**(4), pp. 356-358.

19. Landau, L. D. and Lifshitz, E. M., 1959, *Fluid Mechanics*, vol. 6, Pergamon Press, Massachusetts.

20. London, F., 1954, *Superfluids*. vol. 2, John Wiley & Sons, INC, New York, NY.

21. Lundgren, T.S., *Linearly forced isotropic turbulence*, in Annual Research Briefs (Center for Turbulence Research, Stanford, 2003), pp. 461–473.

22. Mathews, J. K. and Fink, K. K., 2004, *Numerical Methods Using Mathlab*, ed 4th, Prentice-Hall, Upper Saddle River, NJ.

23. Moin, P., 2001, *Fundamentals of Engineering Numerical Analysis*. Cambridge University Press, Cambridge, UK.

24. Niemela, J. J., Sreenivasan, K. R., and Donnelly, R., 2005, *Grid Generated Turbulence in Helium II*, J. Low Temp. Phys., **138**(3), pp. 537-542.

25. Nore, C., Abid, M., and Brachet, M. E., 1997, *Kolmogorov Turbulence in Low-Temperature Superflows,* Phys. Rev. Lett., **78**(20), pp 3896-3899.

26. Orszag, S. and Patterson, G. S., 1972, *Numerical Simulation of Three-Dimensional Homogeneous Isotropic Turbulence*, Phys. Rev. Lett., **28**(2), pp. 76-79.

27. Pope, S. B., 2000, *Turbulent Flow,* Cambridge University Press, New York, NY.

28. Press, W., Vetterling, W., Teukolsky, S., and Flannery, B., 1992, *Numerical Recipes in Fortran 77: The Art of Scientific Computing*, 2nd edition, Cambridge University Press, New York, NY.

29. Press, W., Vetterling, W., Teukolsky, S., and Flannery, B., 1999, *Numerical Recipes in Fortran 90: The Art of Scientific Computing*, 2nd edition, Cambridge University Press, New York, NY.

30. Rosales, C., and Meneveau, C., 2005, *Linear forcing in numerical simulations of isotropic turbulence: Physical space implementations and convergence properties*, Phys. Fluids, **17**(9), pp. 095106(8).

31. Rouson, D.W.I. Rosenberg, R., Xu, X., Moulitsas, I., and Kassinos, S. C., 2008, *A Grid-Free Abstraction of the Navier-Stokes Equations via Data Structure Wrappers in Fortran 95/2003*, ACM Trans. Math Softw., **34**(1).

32. Rouson, D.W.I., and Xiong, Yi, 2004, *Design metrics in quantum turbulence simulation: How physics influence software architecture,* Scientific Programming. **12**(3), pp. 185-196.

33. Rouson, D.W.I., Morris, K. and Xu, X., 2005, *Dynamic memory de-allocation in Fortran 95/2003 derived type calculus,* Scientific Programming, **13**, pp. 189-203.

34. Rouson, D.W.I., Xu, X. and Morris, K., 2006, *Formal constraints on memory management in composite overloaded operations*, Scientific Programming, **14**(1), pp. 27-40.

35. Samuels, D. C., 1993, *Response of superfluid vortex filaments to concentrated normal fluid vorticity*, Phys. Rev. B. **47**(2), pp. 1107-1110.

36. Samuels, D. C., and Kivotides, D., 1999, *A Damping Length Scale for Superfluid Turbulence*, Phys. Rev. Lett., **83**(25), pp. 5306-5309.

37. Samuels, D. C., *Vortex Filament Methods for Superfluids,* in *Quantized Vortex Dynamics and Superfluid Turbulence,* edited by C. F. Barenghi, R. J. Donnelly, and W. F. Vinen, Lectures Notes in Physics (Springer, New York, 2001).

38. Samuels, D.C., 1990, *The Sideband Instability and Recurrence of Vortex Waves in Superfluid Helium II*, Ph. D thesis, University of Oregon, Eugene, OR.

39. Schwarz, K. W., 1978, *Turbulence in superfluid helium: Steady homogeneous counterflow*, Phys. Rev. B, **18**(1), pp. 245-262.

40. Schwarz, K. W., 1982, *Generation of Superfluid Turbulence Deduced from Simple Dynamical Rules*, Phys. Rev. Lett., **49**(4), pp. 283-285.

41. Schwarz, K. W., 1985, *Three-dimensional vortex dynamics in superfluid 4He: Line-line and line-boundary interactions*, Phys. Rev. B, **31**(9), pp. 5782-5804.

42. Schwarz, K. W., 1988, *Three-dimensional vortex dynamics in superfluid 4He: Homogeneous superfluid turbulence*, Phys. Rev. B, **38**(4), pp. 2398-2417.

43. Schwarz, K. W., 1990, *Evidence for organized small structures in fully develop turbulence,* Phys. Rev. Lett., **64**(4), pp. 415-418.

44. Smith, M. R., Hilton, D. K., and Van Sciver, S. W, 1999, *Observed drag crisis on a sphere in flowing He I and He II*, Phys. Fluids, **11**(4), pp. 751-753.

45. Spalart, P.R., Moser, R.D. and Rogers, M.M., 1991, *Spectral Methods for Navier-Stokes Equations with One Infinite and Two Periodic Directions*, J. Comput. Phys., **96**, pp. 297-324.

46. Stalp, S. R., Skrbek, L., and Donnelly, R., 1999, *Decay of Grid Turbulence in a Finite Channel*, Phys. Rev. Lett., **82**(24), pp. 4831-4834.

47. Stalp, S.R., Niemela, J. J., Vinen, W. F. and Donnelly, R. J. 2002, *Dissipation of grid turbulence in helium II*, Phys. Fluids, **14**(4), pp. 1377-1379.

48. Taylor, G. I., and Green ,A. E., 1937, *Mechanism of the Production of Small Eddies from Large Ones*, Proceedings of the Royal Society of London. Series A, Mathematical and Physical Sciences, **158**(895), pp.499-521.

49. Tisza, L., 1940, J. de phys. et rad., **1, 165** and **350**.

50. Vinen, W. F. and Niemela, J. J., 2002, *Quantum Turbulence*, J. Low Temp. Phys., **128**(5-6), pp. 167-231.

51. Vinen, W. F., 1956, Proc. Roy. Soc. A, **238**, and **204**.

52. Vinen ,W. F., 1957, Proc. Roy. Soc. A, **240, 114**, and **128**.

53. Xiong, Yi., 2003, Proposal for Second Examination: *Numerical Simulation of Superfluid Turbulence,* City College of The City University of New York, New York, NY.